



UNIVERSITÀ DEGLI STUDI DI PADOVA

Dipartimento di Fisica e Astronomia “Galileo Galilei”

Master Degree in Physics

Final Dissertation

**Measurement of the time-integrated mixing probability for  
neutral B mesons with CMS**

Thesis supervisor

Prof. Franco Simonetto

Thesis co-supervisor

Dr. Enrico Lusiani

Candidate

Arianna Pajola

Academic Year 2024/25



# Contents

<b>1</b>	<b>Introduction</b>	<b>4</b>
<b>2</b>	<b>Meson mixing formalism</b>	<b>5</b>
2.1	Time integrated mixing probability . . . . .	9
2.2	Mixing measurements . . . . .	11
<b>3</b>	<b>The Large Hadron Collider</b>	<b>12</b>
3.1	The Compact Muon Solenoid . . . . .	12
3.2	Tracker . . . . .	14
3.3	Electromagnetic calorimeter . . . . .	15
3.4	Hadronic calorimeter . . . . .	16
3.5	Muon system . . . . .	16
3.6	Trigger system . . . . .	18
3.7	CMS coordinate system . . . . .	19
<b>4</b>	<b>Data analysis</b>	<b>20</b>
4.1	Trigger . . . . .	21
4.2	Event simulation . . . . .	22
4.3	Event reconstruction and selection . . . . .	23
4.4	Sample compositions . . . . .	24
4.5	Analysis method . . . . .	27
4.5.1	Direct and background muons . . . . .	28
4.5.2	Correlated and uncorrelated muons . . . . .	33
4.5.3	A simulation study of DGS events . . . . .	36
4.6	Fitting procedure . . . . .	40
4.7	Check on MC . . . . .	42
4.8	Final fit and $\bar{\chi}$ estimate . . . . .	44
4.9	Cross check on uncorrelated muons . . . . .	49
<b>5</b>	<b>Conclusions</b>	<b>50</b>
<b>A</b>	<b>Cascade background characterization</b>	<b>52</b>
<b>B</b>	<b>Pile-up analysis</b>	<b>55</b>
<b>C</b>	<b>Multivariate Analysis (MVA)</b>	<b>57</b>
C.1	Boosted decision trees . . . . .	57

# 1 Introduction

This thesis work aims to measure the time-integrated mixing probability  $\bar{\chi}$  of neutral B mesons produced in pp collisions at the LHC collider and recorded by the CMS experiment. The phenomenon of mixing, or oscillation, describes the transformation of a neutral meson into its antiparticle and has been observed for neutral kaons, D and B mesons.

From a measurement of the mixing parameter  $\bar{\chi}$ , we want to obtain an estimate of the production fractions  $f_d$  and  $f_s$ ; these parameters represent the fractions of  $B^0$  and  $B_s^0$  mesons produced in an unbiased sample of weakly decaying b-hadrons produced in high-energy collisions, and are important input parameters for many analysis, including the challenging measurement of the branching ratio  $Br(B_s^0 \rightarrow \mu\mu)$ .

Because of the large b-quark production cross section in pp collisions, an abundant data set is available with the data collected during Run2.

The method here described is a novel way to perform this type of measurement at LHC, since it provides an estimate of the production fractions without relying on the knowledge of specific branching ratios, which are generally difficult to measure at hadron colliders.

## 2 Meson mixing formalism

The phenomenon of mixing, or oscillation, describes the transformation of a neutral meson into its antiparticle and is mediated by the weak interactions. Since weak interactions violate the flavor (F) symmetry,  $\Delta F = 2$  transitions are allowed and these processes are described by the Flavor-Changing Neutral Currents (FCNC).

In the Standard Model, FCNC are not present at tree level because of the structure of the neutral interactions (i.e. mediated by the Z boson), which are diagonal and flavor-conserving. These processes are possible only at one-loop level (or at higher orders) and can be described through box diagrams with charged mediators. The process of oscillation has been observed for kaons, D and B mesons.

A depiction of the Feynman diagrams for the oscillation of a neutral B meson is reported, with  $q=(d, s)$  and  $u_i=(u, c, t)$ :



Since the element of the  $V_{CKM}$  matrix (Cabibbo-Kobayashi-Maskawa matrix, [2]) verify  $|V_{tb}| \gg |V_{ts}| \gg |V_{td}|$ , and the masses of the up-type quarks  $u_i$  verify  $m_t \gg m_c, m_u$ , among all the possible contributions only the box diagrams involving two top quarks contribute significantly to the mixing process.

The oscillation of neutral B mesons can be described by an open state written as a linear combination of the two orthogonal states  $|B_q^0\rangle$  (meson) and  $|\bar{B}_q^0\rangle$  (anti-meson) that evolves in time following the Hamiltonian of the process. This non-Hermitian Hamiltonian  $\mathcal{H}$  is written as the sum of two 2x2 hermitian matrices  $M$  and  $\Gamma$ , both with non-zero off-diagonal components. The off-diagonal terms  $M_{12} = M_{21}^*$  are proportional to the mesons oscillation amplitudes, while  $\Gamma_{12} = \Gamma_{21}^*$  accounts for the interference between the decays of the  $|B_q^0\rangle$  and  $|\bar{B}_q^0\rangle$  components of the time-evolved state. Moreover, due to CPT invariance  $M_{11} = M_{22} = M$  and  $\Gamma_{11} = \Gamma_{22} = \Gamma$ .

$$\mathcal{H} = M - \frac{i}{2}\Gamma = \begin{pmatrix} M - \frac{i}{2}\Gamma & M_{12} - \frac{i}{2}\Gamma_{12} \\ M_{12}^* - \frac{i}{2}\Gamma_{12}^* & M - \frac{i}{2}\Gamma \end{pmatrix}$$

Unlike other meson systems, there are a large number of B-meson decay modes, to which only a few are common to both  $B_q^0$  and  $\bar{B}_q^0$ , so the contribution to the Hamiltonian from the interference between the decays of the  $B_q^0$  and  $\bar{B}_q^0$  is small,  $\Gamma_{12}, \Gamma_{21} \ll \Gamma$ . After the diagonalization of the Hamiltonian the two mass eigenstates  $B_{q,L}$  and  $B_{q,H}$  can be defined

as

$$|B_{q,L}\rangle = p |B_q^0\rangle + r |\bar{B}_q^0\rangle \quad |B_{q,H}\rangle = p |B_q^0\rangle - r |\bar{B}_q^0\rangle$$

with masses

$$m_L = M - |M_{12}| \quad m_H = M + |M_{12}|$$

and where

$$\frac{r}{p} = \pm \left( \frac{M_{12}^*}{M_{12}} \right)^{1/2}$$

The average lifetimes of the  $B^0$  ( $\bar{b}d$ ) and the  $B_s^0$  ( $\bar{b}s$ ) mesons are, respectively, [31]:

$$\tau_d = \Gamma_d^{-1} = (1.517 \pm 0.004) \text{ ps} \quad \tau_s = \Gamma_s^{-1} = (1.516 \pm 0.006) \text{ ps}$$

For the  $B^0$  meson, the light and heavy mass eigenstates have approximately the same width,

$$\Delta\Gamma_d/\Gamma_d = (0.1 \pm 1.0) \cdot 10^{-2}$$

For the two eigenstates of the  $B_s^0$ , instead, the width difference is measured to be

$$\Delta\Gamma_s/\Gamma_s = 0.124 \pm 0.07$$

The mass eigenstates of the Hamiltonian can be rewritten as function of the parameter  $\xi_q = M_{12}^*/|M_{12}|$  as follows

$$|B_{q,L}\rangle = \frac{1}{\sqrt{1+|\xi_q|^2}} [ |B_q^0\rangle + \xi_q |\bar{B}_q^0\rangle ] \quad |B_{q,H}\rangle = \frac{1}{\sqrt{1+|\xi_q|^2}} [ |B_q^0\rangle - \xi_q |\bar{B}_q^0\rangle ]$$

As there is yet no experimental evidence of CP violation induced by mixing in the neutral B meson system,  $|\xi_q| \approx 1$ ; hence, the physical states of the neutral B-meson can be written as

$$|B_{q,L}\rangle = \frac{1}{\sqrt{2}} [ |B_q^0\rangle + e^{i\phi} |\bar{B}_q^0\rangle ] \quad |B_{q,H}\rangle = \frac{1}{\sqrt{2}} [ |B_q^0\rangle - e^{i\phi} |\bar{B}_q^0\rangle ] \quad (1)$$

Supposing now that a  $B_q^0$  is produced at a time  $t = 0$ , the flavor state can be expressed in terms of the physical  $B_{q,H}$  and  $B_{q,L}$  mass eigenstates

$$|B_q^0\rangle = \frac{1}{\sqrt{2}} [ |B_{q,L}\rangle + |B_{q,H}\rangle ] .$$

The wavefunction evolves according to the time dependence of the physical states

$$|B_q(t)\rangle = \frac{1}{\sqrt{2}}[\theta_{q,L}(t)|B_{q,L}\rangle + \theta_{q,H}(t)|B_{q,H}\rangle] . \quad (2)$$

where the time dependencies of the physical states are

$$\theta_{q,L} = e^{-\Gamma_q t/2} e^{-im_L t} \quad \text{and} \quad \theta_{q,H} = e^{-\Gamma_q t/2} e^{-im_H t}$$

The state in Eq:2 can be expressed in terms of the flavor eigenstates using Eq:1; from that the probabilities of the state  $B_q(t)$  to decay as  $|B_q^0\rangle$  or  $|\bar{B}_q^0\rangle$  are extracted:

$$P(B_q^0, t=0 \rightarrow B_q^0) = |\langle B_q^0 | B_q(t) \rangle|^2 = e^{-\Gamma_q t} \cos^2 \left( \frac{1}{2} \Delta m_q t \right)$$

$$P(B_q^0, t=0 \rightarrow \bar{B}_q^0) = |\langle \bar{B}_q^0 | B_q(t) \rangle|^2 = |\xi_q|^2 e^{-\Gamma_q t} \sin^2 \left( \frac{1}{2} \Delta m_q t \right)$$

where the mass difference is computed as  $\Delta m_q = m(B_{q,H}) - m(B_{q,L})$ .

The corresponding expressions for a state that was produced as a  $\bar{B}_q^0$  are

$$P(\bar{B}_q^0, t=0 \rightarrow \bar{B}_q^0) = |\langle \bar{B}_q^0 | B_q(t) \rangle|^2 = e^{-\Gamma_q t} \cos^2 \left( \frac{1}{2} \Delta m_q t \right)$$

$$P(\bar{B}_q^0, t=0 \rightarrow B_q^0) = |\langle B_q^0 | B_q(t) \rangle|^2 = \left| \frac{1}{\xi_q} \right|^2 e^{-\Gamma_q t} \sin^2 \left( \frac{1}{2} \Delta m_q t \right)$$

Recalling that  $|\xi_q| \approx 1$ ,

$$P(B_q^0, t=0 \rightarrow B_q^0) = P(\bar{B}_q^0, t=0 \rightarrow \bar{B}_q^0) \quad \text{and} \quad P(B_q^0, t=0 \rightarrow \bar{B}_q^0) \approx P(\bar{B}_q^0, t=0 \rightarrow B_q^0)$$

As the oscillation probabilities depend on  $\Delta m_q$ , from the time-dependent analysis of the flavor-tagged mesons, the mass difference can be measured: the flavor of the mesons is tagged at production and at decay, and oscillated and non-oscillated particles are counted as function of the proper time.

The values of  $\Delta m_q$  obtained at the LHCb experiment from the analysis of the decay time distributions of  $B^0$  [15] and  $B_s^0$  [10] are:

- $\Delta m_d = (505.0 \pm 2.1(\text{stat}) \pm 1.0(\text{syst})) \text{ ns}^{-1}$
- $\Delta m_s = (17.768 \pm 0.023(\text{stat}) \pm 0.006(\text{syst})) \text{ ps}^{-1}$

For the  $B^0$  meson (Fig:1), the oscillation time scale and the decay time are of the same order of magnitude,  $\Delta m_d/\Gamma_d \approx 1$ . For the  $B_s^0$  instead, (Fig:2) the oscillation time scale is smaller than the particle mean life,  $\Delta m_s/\Gamma_s \gg 1$ , and the results is that more periods of oscillation are visible.

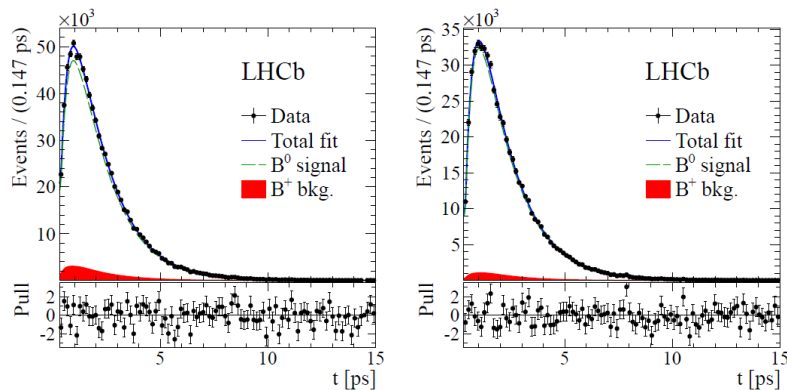


Figure 1: Decay time distributions for  $B^0 \rightarrow D^- \mu^+ \nu_\mu X$  (left) and  $B^0 \rightarrow D^{*-} \mu^+ \nu_\mu X$  (right) in the category with lowest mistag in 2012 data. [15].

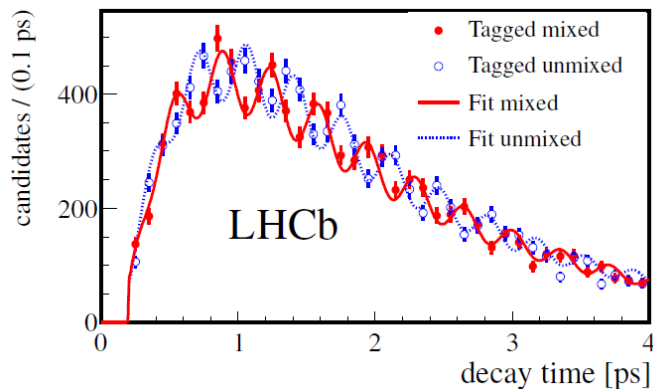


Figure 2: Decay time distribution for the sum of the five decay modes for candidates tagged as mixed (different flavor at decay and production; red, continuous line) or unmixed (same flavor at decay and production; blue, dotted line). The data and the fit projections are plotted in a signal window around the reconstructed  $B_s^0$  mass of 5.32 - 5.55  $\text{GeV}/c^2$ . [10].

## 2.1 Time integrated mixing probability

The aim of this work is to perform a time-integrated measurement, rather than to observe the oscillation paths or to measure  $\Delta m_q$ .

To achieve this, we define the time-integrated mixing probabilities as

$$\chi_q^+ = \int_0^\infty P(B_{q,(t=0)}^0 \rightarrow \bar{B}_q^0) dt \quad \text{and} \quad \chi_q^- = \int_0^\infty P(\bar{B}_{q,(t=0)}^0 \rightarrow B_q^0) dt$$

and their combination, the *average time-integrated mixing probability*, is defined as

$$\chi_q = \frac{\chi_q^+ + \chi_q^-}{2} = \frac{\Delta m_q^2 + \Delta \Gamma_q^2/4}{2(\Delta m_q^2 + \Gamma_q^2)}$$

In proton-proton collisions at the LHC two kinds of weakly decaying neutral b-mesons are produced,  $B^0$  ( $\bar{b}d$ ) and  $B_s^0$  ( $\bar{b}s$ ) (the corresponding antiparticles are implied), so the former probability can be written as the sum of the two contributions:

$$\bar{\chi} = f_d \chi_d + f_s \chi_s$$

The parameters  $\chi_{d,s}$  are the individual mixing probabilities, which are obtained by integrating the measurements of  $\Delta m_{d,s}$  and  $\Delta \Gamma_{d,s}$ . Their values have been measured very precisely by different experiments and have been combined by the HFLAV averaging group to give the following values: [30]

- $\chi_d = 0.1860 \pm 0.0011$ , from all ALEPH, DELPHI, L3, OPAL, CDF, D0, BABAR, BELLE, LHCb, ARGUS and CLEO measurements;
- $\chi_s = 0.499314 \pm 0.000005$  from CDF, LHCb, CMS measurements.

The parameters  $f_{d,s}$  are the **production fractions**, defined as the fractions of  $B^0$  and  $B_s^0$  in an unbiased sample of weakly decaying b-hadrons produced in high-energy collisions. The latest results of the measurement of the mixing probability and production fractions provided by the HFLAV group are reported in Tab:1

It would be tempting to assume that the fractions of different species in unbiased samples of b-hadrons are independent of whether they originated from  $e^+e^-$  collisions, pp collisions at the Tevatron or pp collisions at the LHC.

However, data show that this hypothesis is only verified for high energy events ( $p_T > 20$  GeV), in which the production mechanism of a b hadron is completely described by the fragmentation of the b quark. For smaller values, there are interference effects between the production mechanism of the b quark, which are different at hadron and high-energy lepton colliders, and its hadronization, which is expected to be process-independent.

Quantity		LEP	Tevatron	ATLAS	LHCb
Mixing probability	$\chi$	$0.1259 \pm 0.0042$	$0.147 \pm 0.011$		
$B^+$ or $B^0$ fraction	$f_u = f_d$	$0.407 \pm 0.007$	$0.344 \pm 0.021$		
$B_s^0$ fraction	$f_s$	$0.101 \pm 0.008$	$0.115 \pm 0.013$		
$b$ -baryon fraction	$f_{baryon}$	$0.085 \pm 0.011$	$0.198 \pm 0.046$		
$B_s^0/B^0$ ratio	$f_s/f_d$	$0.249 \pm 0.023$	$0.334 \pm 0.040$	$0.240 \pm 0.020$	$0.256 \pm 0.020$

Table 1: Time-integrated mixing probability  $\bar{\chi}$ , and production fractions of the different b-hadron species in an unbiased sample of weakly decaying b hadrons, obtained from both direct and mixing measurements. [23]

An analysis [29] of the CMS experiment shows that the value of the parameter

$$R_S = \frac{f_s}{f_u} \frac{Br(B_s^0 \rightarrow J/\Psi\phi) \cdot Br(\phi \rightarrow K^+K^-)}{Br(B^+ \rightarrow J/\Psi K^+)}$$

and consequently of the single production fractions, depends on the transverse momentum, as visible in Fig:3. This is consistent with a previous observation of LCHb [21], which spans a different range in rapidity and transverse momentum.

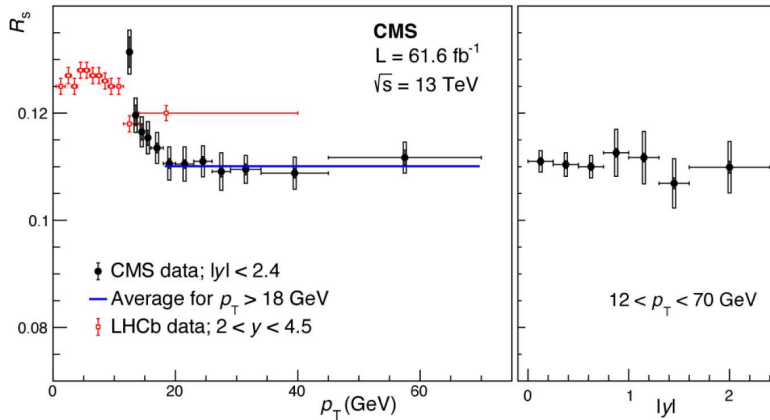


Figure 3: Measurement of the parameter  $R_S \propto \frac{f_s}{f_u}$ , in bins of transverse momentum (left) and rapidity (right). A clear dependence with the  $p_T$  is present.

A measurement of  $\bar{\chi}$  therefore allows to put a constraint between the values of  $f_d$  and  $f_s$ , independent on the knowledge of  $B^0$  and  $B_s^0$  branching fractions. The analysis is performed in bins of  $p_T$  (see Sect:4.5.1 for details) in order to qualitatively compare it with Fig:3 and with the LEP measurement.

## 2.2 Mixing measurements

In order to measure the oscillation probability, it is necessary to determine the flavor of the system at the time of the b-quark production and of the B-meson decay.

The flavor at decay time is usually determined by looking at the charge of some of the final state particles, like a high  $p_T$  lepton or the charge of a reconstructed charm particle. The way to determine the flavor at production time, instead, depends on whether the  $b\bar{b}$  pair is produced as a coherent or incoherent state.

If the  $b\bar{b}$  system is produced at b-factories, where the  $e^+e^-$  annihilation occurs at the  $\Upsilon(4S)$  resonance, the correlation is present between the two B mesons that are produced, so that they will hadronize as a  $B^0\bar{B}^0$  or  $B^+B^-$  pair. The  $b\bar{b}$  pair produced from the decay of the resonance is as an entangled state in the  $L = 1$  wavefunction. The first meson to decay tags the flavors of the other B (which must be opposite) at that time. The surviving state can then propagate for an additional time  $\Delta t$ , and only during this time it can possibly oscillate.

For the production at the LEP collider or at the LHC, instead, the  $b\bar{b}$  pair is produced with an energy well above the resonance threshold and the correlation is present only at the quark level:  $b$  and  $\bar{b}$  are produced in pairs to preserve the flavor, but then they independently hadronize in different B mesons or baryons and evolve independently. Time integrated mixing measurements at high energy colliders (either LEP or Tevatron) have been performed selecting events with two high energy leptons, and comparing the rates of events with two same-charge leptons ("mixed" events) to opposite-charge ("unmixed"). Neglecting background, the rate  $R_{\text{sc}}$  of equal-charge dileptons to the total number of dilepton events is related to  $\bar{\chi}$  by the following relation:

$$R_{\text{sc}} = \frac{\mathcal{N}^{\pm\pm}}{\mathcal{N}^{\pm\pm} + \mathcal{N}^{\pm\mp}} = 2\bar{\chi}(1 - \bar{\chi})$$

In this work a novel method is presented which exploits a large data set triggered for CP-violation studies. The sample contains a  $B^+$  (reconstructed in the  $J/\Psi(\mu\mu)K^+$  final state) and an additional muon. The flavor of the charged B tags the flavor of the other b at production time, the charge of the muon tags it at decay time. As the charged B does not oscillate, the fraction of same-charge events provides directly the value of  $\bar{\chi}$ :  $R_{\text{sc}} = \bar{\chi}$

### 3 The Large Hadron Collider

The Large Hadron Collider (LHC) [7] is the world’s largest and most powerful particle accelerator. It consists of a 27-kilometer two-ring, superconducting accelerator and collider with four crossing points, where experiments with different structures and purposes, among which the Compact Muon Solenoid (CMS), are positioned. It was designed to collide proton and heavy ion beams with a center-of-mass energy of the order of the TeV and a designed peak luminosity of  $\mathcal{L} = 10^{34} \text{ cm}^{-2} \text{ s}^{-1}$ .

The collider is supplied with protons from a pre-accelerating system, aiming at gradually increasing the energy of the particles. In particular, this chain involves the LINear ACcelerator 2 (LINAC2), the Proton Synchrotron Booster (PSB), Proton Synchrotron (PS) and Super Proton Synchrotron (SPS), from which the protons enter the LHC ring with an energy of 450 GeV.

Some relevant parameters of the beam inside the collider are listed in Tab:2

Parameter	Run2	Nominal
Energy [TeV]	6.5	7.0
Revolution frequency ( $f_{\text{rev}}$ ) [kHz]	11.245	11.245
Beta-function ( $\beta^*$ ) [cm]	30 $\rightarrow$ 25	55
$N_b$ (number of bunches)	2556	2808
$N_p$ (protons per bunch)	$1.1 \cdot 10^{11}$	$1.15 \cdot 10^{11}$
Normalized emittance $\epsilon_n$ [ $\mu\text{m}$ ]	1.9	3.75
Max peak luminosity [ $\text{cm}^{-2} \text{ s}^{-1}$ ]	$2.1 \cdot 10^{34}$	$1.0 \cdot 10^{34}$

Table 2: Beam parameters in the configuration of the LHC design report and in the Run2 configuration achieved in 2018 [19]. The arrow indicates a change during the data taking.

In particular, in this work we will analyze data acquired during Run2, which started in June 2015 and finished in November 2018, for a total delivered luminosity of  $163 \text{ fb}^{-1}$  (Fig:4).

#### 3.1 The Compact Muon Solenoid

The Compact Muon Solenoid detector ([9]) is a multipurpose apparatus that operates at the LHC at CERN. During Run2, it collected head-on collisions of two proton beams with a center of mass energy of 13 TeV. The CMS detectors use several technologies for particle detection and reconstruction and its internal structure is shown in Fig:5.

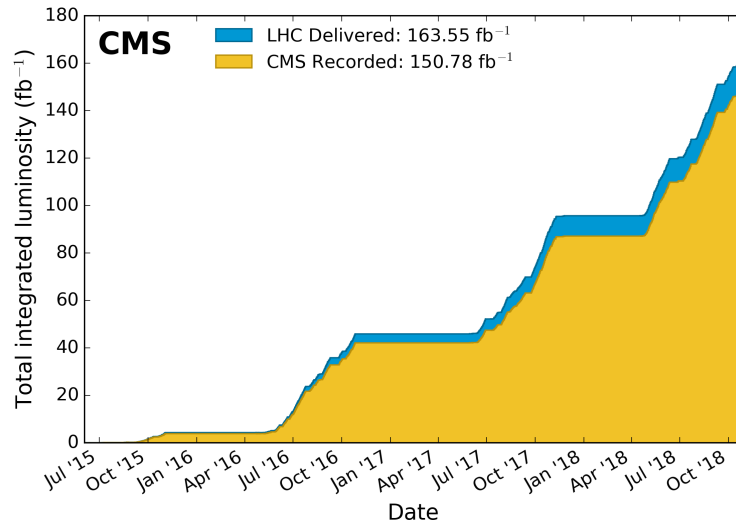


Figure 4: Cumulative delivered and recorded luminosity versus time for 2015-2018, for pp collisions.

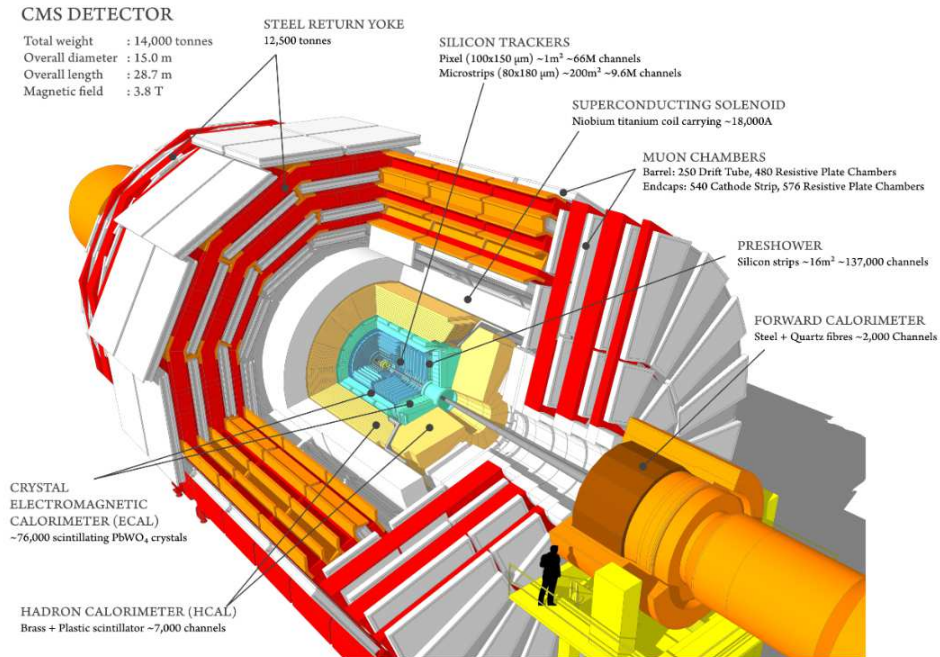


Figure 5: Depiction of the internal structure of the CMS detector.

From the innermost part towards the outside, the silicon tracker reconstructs the trajectories of charged particles, the Electromagnetic Calorimeter (ECAL) and Hadron Calorimeter (HCAL) measure the energy of electromagnetic particles and hadrons, while the muon system occupies the most external part of the CMS detector outside the superconducting solenoid. The latter is a redundant system for muon detection based on three different gaseous detector technologies, as Drift Tubes (DTs), Cathode Strip Chambers (CSCs), and Resistive Plate Chambers (RPCs). At the heart of CMS a 13-m long, 6-m-inner-diameter, 4 T superconducting solenoid provides a large bending power (12 Tm) before the muon bending angle is measured by the muon system. The field is closed by a 104 t iron return yoke made of five barrels and two end caps, composed of three layers each.

### 3.2 Tracker

The CMS tracking system [9] is made of an inner pixel tracker and a silicon strip tracker, covering a pseudo-rapidity range up to  $|\eta| = 2.5$ . (Fig:6)

The pixel tracker comprises approximately 66 million silicon pixel cells with dimensions  $100 \times 150 \mu\text{m}^2$ , allowing a spatial resolution of  $10 \mu\text{m}$  in the  $r$ - $\phi$  plane and around  $15 \mu\text{m}$  in the  $z$  direction. Such a small resolution is needed for an accurate track reconstruction and for the determination of primary and secondary interaction vertices. A new pixel detector was installed in 2017 [20], equipped with one additional barrel layer and one additional forward disk. In the new pixel detector, the innermost layer is closer to the interaction point and the outermost one is further away from it, to assure the best resolution on the vertex reconstruction.

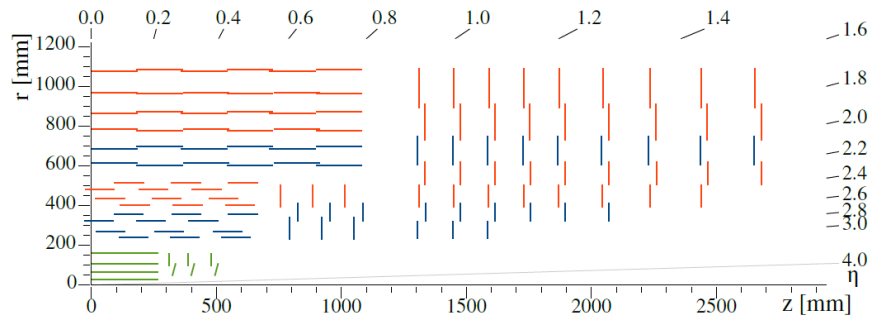


Figure 6: Sketch of one quarter of the tracking system in  $r$ - $z$  view. The pixel detector is shown in green, while single-sided and double-sided strip modules are depicted as red and blue segments, respectively. [18]

The silicon strip tracker is composed of silicon modules that carry one or two silicon sensors. In the barrel region, the modules are arranged in ten layers, extending up to a radius of 1.1 m.

In the barrel, the strips are oriented along the  $z$  direction, while in the endcaps they are oriented along the  $r$  direction. This layer is designed to provide a spatial resolution of approximately  $20\text{-}50\ \mu\text{m}$  in the  $r\text{-}\phi$  plane and between  $200\text{-}500\ \mu\text{m}$  along the  $z$  direction. Since 2017, they have been operated at a lower temperature ( $-20\ \text{°C}$ ) to mitigate long-term damage and guarantee a good signal-to-noise ratio.

The tracker provides a momentum resolution of  $0.5\% \oplus 15\% \cdot p_T$  [TeV] in the central region with  $|\eta| < 1.6$ , degrading to  $0.5\% \oplus 60\% \cdot p_T$  [TeV] as  $|\eta|$  approaches 2.5.

### 3.3 Electromagnetic calorimeter

The electromagnetic calorimeter of CMS (ECAL) [9] is a hermetic homogeneous calorimeter made of 61200 lead tungstate ( $\text{PbWO}_4$ ) crystals mounted in the central barrel part, closed by 7324 crystals in each of the two endcaps. A preshower detector is placed in front of the endcap crystals. Avalanche photodiodes are used as photodetectors in the barrel, while vacuum phototriodes are used in the endcaps. The use of high density crystals has allowed the design of a calorimeter which is fast, has fine granularity and is radiation resistant, all important characteristics in the LHC environment. This capability is enhanced by the good energy resolution provided by a homogeneous crystal calorimeter and described by the following formula:

$$\left(\frac{\sigma}{E}\right)^2 = \left(\frac{S}{\sqrt{E}}\right)^2 + \left(\frac{N}{E}\right)^2 + C^2 = \left(\frac{2.8\%}{\sqrt{E}}\right)^2 + \left(\frac{12\%}{E}\right)^2 + (0.3\%)^2$$

where  $S$  is the stochastic term,  $N$  accounts for the noise from the electronics and  $C$  is the term related to crystal inhomogeneities and calibration effects.

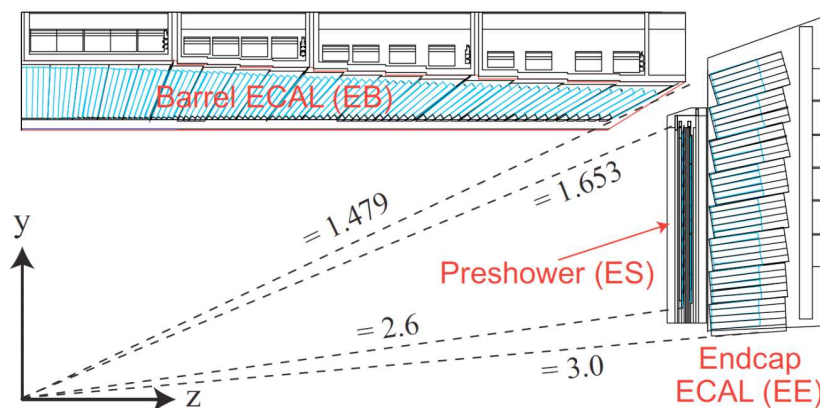


Figure 7: Section of the ECAL in the  $y\text{-}z$  plane. [12]

### 3.4 Hadronic calorimeter

The central hadron calorimeter [9], divided into the Hadron calorimeter Barrel (HB) and End cap (HE), is a sampling calorimeter using a brass absorber and plastic scintillator tiles. In addition, the HB calorimeter is complemented with an Outer calorimeter (HO) positioned outside the cryostat and inside the magnetic flux return yoke. A separate Forward calorimeter (HF) is located 6 m downstream of the HE ( $|z|=11$  m) at  $2.9 < |\eta| < 5.0$  to extend the hermeticity of the central hadron calorimeter to higher pseudorapidity. It uses a steel absorber and detects light from scintillating quartz fibers. In 2017 the readout was upgraded with new PhotoMultiplier Tubes with dual readout and upgraded electronics, allowing better discrimination of real hits from muons hitting the PMT window. In the HE, the readout previously made with Hybrid PhotoDetectors was completely upgraded with Silicon PhotoMultipliers, which allow finer longitudinal segmentation and improved photodetection efficiency.



Figure 8: Section of the HCAL showing the locations of the hadron barrel (HB), endcap (HE), outer (HO) and forward (HF) calorimeters. [9]

### 3.5 Muon system

Muon detection is a powerful tool for recognizing signatures of interesting processes over the very high background rate expected at the LHC with full luminosity, therefore the detection of muons is of central importance to CMS. The muon system has 3 functions: muon identification, momentum measurement, and triggering. Good muon momentum

resolution and trigger capability are enabled by the high-field solenoidal magnet and its flux-return yoke. The latter also serves as a hadron absorber for the identification of muons. In the barrel region, where the neutron-induced background is small, the muon rate is low, and the 4-T magnetic field is uniform and mostly contained in the steel yoke, drift chambers with standard rectangular drift cells are used. The barrel drift tube (DT) chambers cover the pseudorapidity region  $|\eta| < 1.2$  and are organized into 4 stations arranged among the layers of the flux return plates.

In the 2 endcap regions of CMS, where the muon rates and background levels are high and the magnetic field is large and non-uniform, the muon system uses cathode strip chambers (CSC). With their fast response time, fine segmentation, and radiation resistance, the CSCs identify muons between  $|\eta|$  values of 0.9 and 2.4. There are 4 stations of CSCs in each endcap, with chambers positioned perpendicular to the beam line and placed between the flux return plates. The cathode strips of each chamber run radially outward and provide a precision measurement in the  $r$ - $\phi$  bending plane. The anode wires are perpendicular to the strips and are also read out in order to provide measurements of  $\eta$  and the beam-crossing time of a muon. Each 6-layer CSC provides robust pattern recognition for rejection of non-muon backgrounds and efficient matching of hits to those in other stations and to the CMS inner tracker.

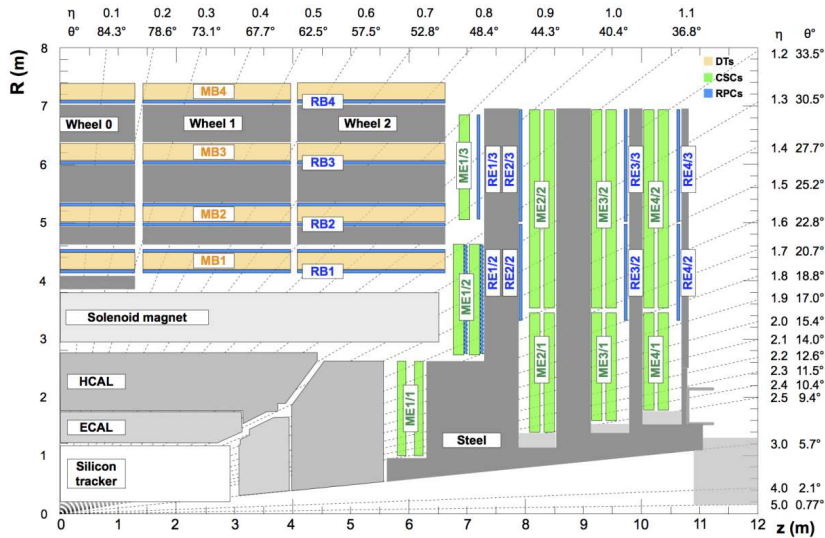


Figure 9: An  $r$ - $z$  cross section of a quadrant of the CMS detector. The locations of the various muon stations and the steel flux-return disks (dark areas) are shown. The DTs are labeled as MB (“Muon Barrel”) and the CSCs are labeled as ME (“Muon Endcap”). RPCs are mounted in both the barrel and endcaps of CMS, where they are labeled as RB and RE, respectively. [13]

As electrons and charged hadrons are absorbed in the calorimeters, muon tagging is performed by matching a track reconstructed in the silicon with the segment reconstructed in the muon chambers. To enhance the rejection of sail-through and punch-through hadrons, a tighter selection is applied, which combines information from the two tracking systems in a neural network [24]. The output of the network ("htag") is shown in Fig:10 for real muons and hadron tracks.

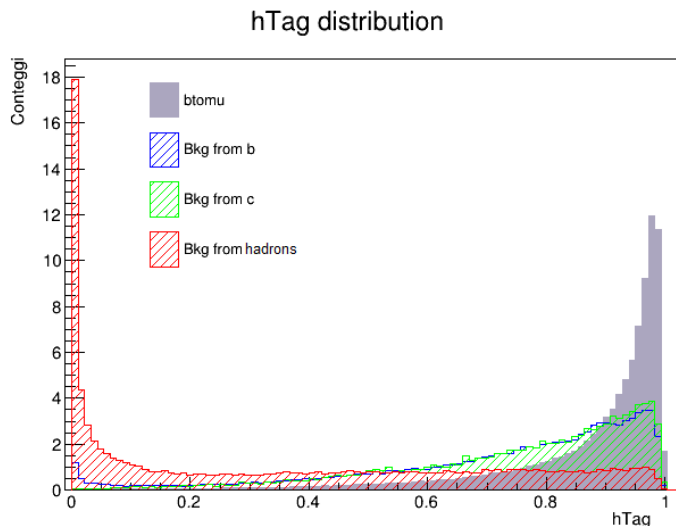


Figure 10: Distribution of the "htag" discriminator for hadrons.

### 3.6 Trigger system

The trigger system reduces the amount of collected data by selecting only interesting events. Given the very high rate of the collisions it would be impossible to store all the recorded events, but most of them are dominated by soft QCD interactions, thus they are not of primary interest and can be discarded.

The trigger system is composed of two stages:

1. the Level 1 (L1) trigger, a hardware-based trigger in which the acquired rate is reduced from the 40 MHz of the bunching cross down to 100 kHz by exploiting information from in the calorimeters and the muon systems.
2. the High-Level Trigger (HLT) combines the information from all the CMS sub-detectors to further reduce the rate to 1 kHz.

Finally, the selected data are divided into different subsets, called primary data sets, based on the triggered objects and the kinematic of the event. The set of selection criteria required for an event to be accepted in a primary data set is called the trigger path.

### 3.7 CMS coordinate system

As is customary in collider physics, a particle is characterized by its mass, its electric charge and its kinematic parameters. CMS employs a cartesian coordinate system, with center in the detector center, z axis along the beam direction, x axis pointing to the center of LHC and y axis perpendicular to both and pointing upward. Consequently, a spherical coordinate system is also defined. The polar angle  $\theta$  is measured from the z axis and the azimuthal angle  $\phi$  is measured from the x axis in the (x, y) plane.

The particle three-momentum is usually expressed in terms of its azimuth  $\phi$ , its projection along the (x-y) plain  $p_T$  and its pseudorapidity  $\eta$ , defined as follows:

$$p_T = \sqrt{p_x^2 + p_y^2} \quad \eta = -\ln \left( \tan \frac{\theta}{2} \right) = \frac{1}{2} \ln \left( \frac{|\vec{p}| + p_z}{|\vec{p}| - p_z} \right)$$

where  $|\vec{p}|$  is the magnitude of the three-momentum  $\vec{p} = (p_x, p_y, p_z)$ .

The angular distance between two tracks is defined by the parameter

$$\Delta R = \sqrt{(\phi_1^2 - \phi_2^2)^2 + (\eta_1 - \eta_2)^2}$$

The quantities  $(p_T, \eta, \phi)$  and  $\Delta R$  are invariant under Lorentz boost along the beam axis.

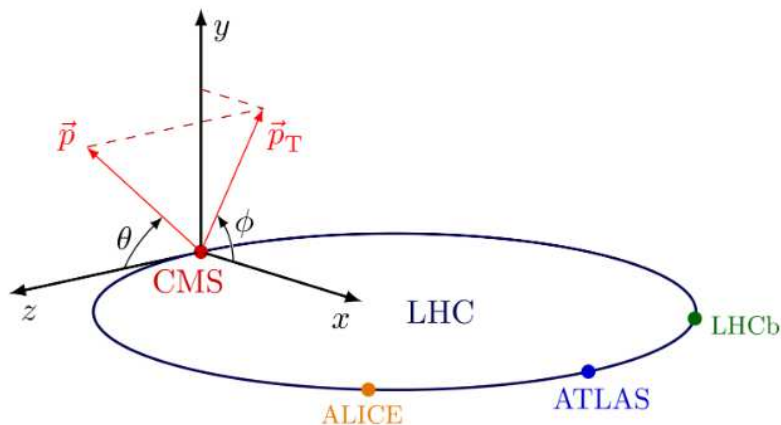


Figure 11: Depiction of the CMS coordinate system. [33]

## 4 Data analysis

The predicted NNLO  $b\bar{b}$  production cross section in proton-proton collisions at  $\sqrt{s} = 13$  TeV is  $\sigma(pp \rightarrow b\bar{b}X) \approx 500 \mu\text{b}$  [25]. With an integrated luminosity  $\mathcal{L} = 163 \text{ fb}^{-1}$  acquired during Run2, a huge number ( $O(10^{14})$ ) of  $b\bar{b}$  pairs is produced. Only a tiny fraction of all the collisions produced at the LHC can however be recorded on disk for further processing: for these purpose only events fulfilling some features decided a priori are selected, by defining proper trigger paths. The trigger employed for this measurement is described in the next paragraph.

For this mixing measurement, we focus in particular on events with a fully reconstructed charged B meson that follows the decay path  $B^+ \rightarrow J/\Psi K^+ \rightarrow \mu^+ \mu^- K^+$  (the conjugate process is implied) and an additional muon. As charged B mesons do not mix, due to charge conservation, from the charge of the B hadron, hereafter the "tag side" hadron ( $B_{tag}$ ), the flavor *at production* of the other b quark of the events, in the "probe side", can be inferred without ambiguity. The charge of the third triggered muon tags then the flavor of the other B-hadron in the event (hereafter called  $B_{probe}$ ) *at decay time*.

A depiction of this process is shown in Fig:12. The charge correlation between the  $B_{tag}$  and the  $\mu_{probe}$  is used to indicate whether mixing occurred: events like  $B^+ \mu^+$  result from the oscillation of a B meson in the probe side, while in the case with  $B^+ \mu^-$  the event is unmixed.

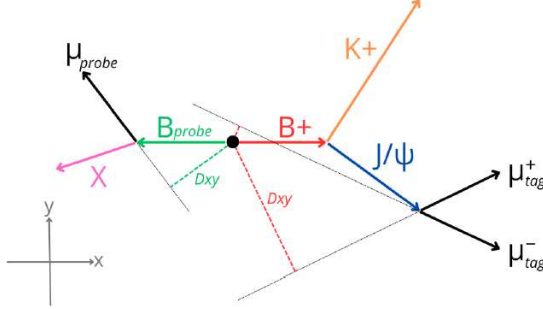


Figure 12: Depiction of the process described above, with the distinction of "tag" and "probe" side. The conjugate process is implied.

From these considerations we can calculate the time-integrated mixing probability as

$$\bar{\chi} = \frac{\mathcal{N}(B^\pm \mu^\pm)}{\mathcal{N}(B^\pm \mu^\pm) + \mathcal{N}(B^\pm \mu^\mp)} \quad (3)$$

This simple picture is spoiled by background events, in which the muon can have either opposite charge correlation or random correlation to the tag hadron. Details on the sample composition are provided below.

## 4.1 Trigger

The trigger used for this analysis is *HLT\_Dimuon0\_Jpsi3p5\_Muon2* [27], hereafter *HLT\_JpsiMu*, that was developed for measurements of CP violation [26]. It requires two muons forming a  $J/\Psi$  vertex and the presence in the event of a third muon, unrelated to the  $J/\Psi$ . The third muon is the tagging muon to be used for the flavor tagging. *HLT\_JpsiMu* selections are summarized in Tab:3 for the L1 trigger and in Tab:4 for the HLT.

*HLT\_JpsiMu* analyzes events with at least three muons that pass the L1 trigger, with the requirements on the highest  $p_T$  and second-highest  $p_T$  muons of  $p_T > 5$  and 3 GeV, respectively, and their invariant mass  $m(\mu_1\mu_2) < 9$  GeV. There is no  $p_T$  requirement on the additional muon at L1. At HLT level, the three muons are required to be within the geometric acceptance of the CMS muon system  $|\eta| < 2.5$  to ensure good reconstruction properties. Two of these muons must have  $p_T > 3.5$  GeV, be oppositely charged, form a  $J/\Psi$  candidate with an invariant mass in the range 2.95–3.25 GeV, and have a probability to originate from a common vertex larger than 0.5%. The third muon is required to have  $p_T > 2$  GeV.

In the offline selection of the events, an additional track compatible with a charged, long-lived hadron is required, representing the kaon emitted by the B hadron.

Variable	L1 requirement
Min. number of muons	3
$p_T(\mu_1)$	$> 5$ GeV
$p_T(\mu_2)$	$> 3$ GeV
$m(\mu_1\mu_2)$	$< 9$ GeV

Table 3: L1 trigger selection requirements of *HLT\_JpsiMu*. The highest  $p_T$  and second-highest  $p_T$  muons are indicated with  $\mu_1$  and  $\mu_2$ , respectively.

Observable	HLT requirement
$ \eta(\mu) $	$< 2.5$
$p_T(\mu^\pm)$	$> 3.5$ GeV
$p_T(\mu_3)$	$> 2$ GeV
$m(\mu^+\mu^-)$	$\in [2.95, 3.25]$ GeV
$J/\psi$ vertex prob.	$> 0.5\%$

Table 4: HLT selection requirements of *HLT\_JpsiMu*. The  $J/\Psi$  candidate is formed by a pair of oppositely charged muons. The muon not used to form the  $J/\Psi$  candidate is indicated with  $\mu_3$ .

## 4.2 Event simulation

In CMS, the simulation of proton-proton collisions is performed in multiple steps. The first step, known as *generation*, involves simulating the physical processes included in the event. The interaction of the two protons is seen as a hard-scattering process of the constituent partons (mainly gluons at  $\sqrt{s} = 13$  TeV) using the so-called “factorization theorem”, in which all interactions with an energy lower than a given factorization scale are absorbed in the parton distribution function <sup>1</sup>, while those with a higher energy are contained in the hard-scattering cross section. From the scattered partons, secondary collinear and soft partons are emitted, progressively degrading the energy and creating the so-called parton shower. Below the renormalization scale, perturbation approaches can no longer be used and hadronization algorithms are implemented to cluster the individual partons of the parton shower into color-singlet hadrons. Particle decays and other probabilistic processes are then generated with fixed physics parameters, which typically correspond to the current world average values.

The second step, called *simulation*, models the response of the detector to a given set of final-state particles. <sup>2</sup> First, the final-state particles are propagated in a full simulation of the CMS detector using the GEANT4 package [6], which models the propagation of particles through the detector layers taking into account all types of interaction with matter, the production of secondary particles, and the influence of electromagnetic fields. Next, the readout of all subsystems is simulated in the digitization step. At this point, the simulation consists of a collection of hits in the tracking and muon systems, and energy deposits in the calorimeters, resembling the detector response for a real collision. Finally, the simulated samples are reconstructed using the same software as the collision data and can be analyzed with common analysis tools. Typically, the simulated samples contain also information on the generated quantities, such as momenta, trajectories, decay time values, as well as decay histories, for the majority of the simulated particles of interest. This enables the development of analysis procedures over labeled data.

The simulated samples used in this work are produced using the PYTHIA 8.240 Monte Carlo event generator [14] with the underlying event tune CP5 [22] and the parton distribution function set NNPDF3.1 [16]. The hadronization algorithm used is the Lund string model [4], as implemented in PYTHIA. Final-state photon radiation is taken into account with PHOTOS 215.5 [3]. The b-hadron decays are modeled with the EVTGEN 1.6.0 package [5].

---

<sup>1</sup>Parton distribution functions describe the probability for a parton to carry a certain momentum fraction of the initial hadron and depend on the type of the scattering parton and the total momentum transferred in the interaction.

<sup>2</sup>Those which live enough as to cross the detector: charged pions, neutral and charged kaons, protons, neutrons, photons, electrons and muons, and their antiparticles. Even if some of them do in fact decay, they are often referred to as “stable particles”

The simulated events are generated by requiring that one of the two B particles hadronize into a  $B^+$ , which then decays into  $J/\Psi K^+$ . In the simulation, this requirement on the tag side also biases events on the probe side, causing a reduction of the number of  $B_{probe}^+$ . However, this is not expected to affect either the dataset or the estimate of the mixing parameter.

### 4.3 Event reconstruction and selection

In order to reconstruct physical objects, the ‘‘Particle Flow’’ (PF) reconstruction algorithm [17] combines the raw information of the CMS sub-detectors into higher-level objects representing stable particles, assigning momentum, energy, direction, and estimating the particle type. The PF algorithm main steps are the following: first, the information from the sub-systems is collected to form the so-called ‘‘PF objects’’. These include tracks of charged particles in the tracking system and in muon detectors and clusters of energy deposited in the calorimeters. Then, the PF objects are spatially correlated with specific *linking algorithms*. Finally, particle hypotheses are inferred and complex objects, such as vertices, jets, and missing energy, are computed.

In this analysis the reconstructed objects are the two opposite charge muons that derive from  $J/\Psi$ , the kaon in the tag side and the muon in the probe side. For approximately 58% of the events the probe muon is not emitted as a standalone but within a jet. These objects, indicated as ‘‘PF-Jets’’, are reconstructed with the anti- $k_T$  algorithm [8], with a radius parameter  $R = 0.4$ . For all the reconstructed objects the charge and the quadrivector are known, together with the coordinates of the interaction vertex in the tag side and the invariant mass of all the particles emitted from it ( $m_V$ ).

For each probe muon a multivariate discriminator ‘‘hTag’’ (which distribution is visible in Fig:10) is defined to separate the background from hadronic particles, i.e. pions or kaons decaying to muons inside the tracker volume (‘‘sail through’’) or hadrons reaching the muon chambers without interacting with the detector material (‘‘punch through’’), that are misidentified as muons. This variable is built using information from silicon trackers and the muon chambers placed in the steel return-yoke (in Fig:9 the structure of the muon chamber is visible).

In the offline selection, the following requirements apply to both data and simulation:

- $p_T > 2$  GeV for  $\mu_{probe}$
- $p_{t,Jet} > 10$  GeV for the jet emitted with the muon.  
For reasons that will be explained in Sect:4.5.1, only events in which the jet is reconstructed, hereafter ‘‘Jet’’ events, will be included in the analysis. This requirement selects 58% of the total number of events.

- $hTag > 0.5$ , to minimize the contamination of the hadronic background while keeping a large dataset;
- $m_V \subseteq [5.07 : 5.47]$  GeV , to select events in which the mass of the "tag" vertex belongs to a region around the  $B^+$  hadron mass  $m_{B^+} = (5.2796 \pm 0.0002)$  GeV [32];
- $\Delta R_{(B_{tag}, jet)} > 0.5$  ; this requirement on the angular distance between the tag hadron and the jet that contains the muon is made in order to reject events in which particles belonging to the tag side enter the jet cone.
- Distance of the "tag" and "probe" vertices on the beam axis  $\Delta z = z_{prb} - z_{tag} < 0.25$ , where  $z_{prb}$  is the coordinate along the z direction of the point where the muon track intersects the beam line;  $z_{tag}$  is obtained as the average position along z of the intersections of each track forming the  $B_{tag}$  with the beam line. This requirement is applied to reduce the contamination from events where the probe muon is produced from a collision different from that of the  $B_{tag}$  ("pile-up" events, or "PU"): PU background contributes to about 1% of the whole data-set. PU data, obtained by inverting and tightening this selection, are used as a background control sample. Details are described in Appendix B.

#### 4.4 Sample compositions

Through all the analysis, muons will be identified as:

- "Opposite Charge-OC" if the charge of  $\mu_{probe}$  is opposite to the one of the  $B_{tag}$
- "Same Charge-SC" if the charge of  $\mu_{probe}$  is equal to the one of the  $B_{tag}$
- "All Charge-AC" to include both the previous cases

To better understand the content of the simulation, muons that come from a direct decay of a b quark (kind 1 and 11 in the next paragraph) are listed in Tab:5 according to the hadron from which they originate.

Origin	AC (%)	OC (%)	SC (%)
$B^0$	55.0	53.7	62.4
$B_s$	11.4	6.8	37.4
$B^+, B_c^+$	29.5	34.7	0.2
b barions	4.1	4.8	0.03
# events	270751	229601	41150

Table 5: Sample compositions of  $\mu$  from a direct decay of a b quark, for events with only two B hadrons. As mentioned in the previous paragraph, these numbers are biased by the requirement for a  $B^+ \rightarrow K^+ J/\Psi$  to be produced in each event.

The same percentages are also computed for Jet events only, in Tab:6; since the values correspond well, we verified that the selection of Jet events does not introduce any bias in the sample composition.

Origin	ACJet (%)	OCJet (%)	SCJet (%)
$B^0$	55.0	53.5	63.4
$B_s$	11.3	6.7	36.4
$B^+, B_c^+$	29.6	34.9	0.2
b barions	4.2	4.9	0.03
# events	156148	132293	23855

Table 6: Sample compositions of  $\mu$  from direct decay of a b quark, for Jet events with only two B hadrons.

In the simulation, where it is possible to track the evolution of every event, muons on the probe side are classified with a dedicated variable, "EventKind", according to their origin. In Tab. 7 the production processes that identify different categories are listed, together with the relative contribution of each category, calculated for Jet events that pass the selections criteria described in the previous paragraph.

EventKind	Production process	OCJet events	% OCJet	SCJet events	% SCJet
1-11	$b \rightarrow \mu^- X$	132293	72.99	23855	28.19
2-12	$b \rightarrow c \rightarrow \mu^+ X$	14429	7.96	32935	38.92
3-13	$b \rightarrow \tau^- \rightarrow \mu^- X$	4036	2.23	963	1.14
4-14	$c \rightarrow \mu^+ X, \tau \rightarrow \mu X$	9029	4.98	8467	10.01
5-15	resonances $\eta, \rho, \omega, \phi...$ from b	1002	0.55	950	1.12
6-16	resonances $\eta, \rho, \omega, \phi...$ from light q	219	0.12	261	0.31
7-17	$\pi$ or K from light q	6274	3.46	6387	7.55
8-18	$\pi$ or K from b	1421	0.78	1049	1.24
9-19	other sources	2107	1.16	2069	2.44
PU	residual pile-up	1488	0.76	1489	1.63
DGS	$pp \rightarrow b\bar{b}b\bar{b}X$	8943	4.93	6197	7.32
Total		181241	100	84622	100
Data evts.		154157		67620	

Table 7: Event kind, 1-9 for Opposite Charge and 11-19 for Same Charge. For each category the contributions are shown separately for OC and SC events. The DGS category consists of events with four B hadrons; in this case muons can be correlated or not correlated, as explained in Sect:4.5.3. The number of data events is computed after the blinding procedure, described in Sect:4.6.

The first 9 categories are defined based only on the knowledge of the decay chain in which the muon is emitted. Cases 2 and 12 are defined as "cascade decays" and are particularly obnoxious because the charge correlation of  $B_{tag}$  and  $\mu_{probe}$  is opposite to that of

direct muons, so that they would wrongly assign a "mixed" event as "unmixed" and vice-versa. Appendix A describe a comparison between data and simulated events from cascade.

Pile-up (PU) muons are defined based on the distribution of the  $\Delta z$  variable and they will be analyzed in Appendix B. The residual contribution of pile-up muons after the requirement on  $\Delta z$  has been estimated using the methods detailed there.

The Double Gluon Splitting category (DGS) consists of events in which four B hadrons are generated in the process  $pp \rightarrow b\bar{b}b\bar{b}X$ . Notice that in principle also muons from the category 4-14 can derive from DGS events of the type  $pp \rightarrow b\bar{b}c\bar{c}X$ , but we keep these contributions separate since in this case only two B hadrons are present.

In the simulation, we can tell whether two or four weakly decaying B hadrons are produced, but we do not have enough information, in the case of four, to tell whether the probe muon comes from the b quark related with the  $B_{tag}$  or from a random one. For this reason, the previous table is compiled limiting ourselves to events with only two B hadrons, except for the DGS contribution.

In the simulation, the integrated mixing is calculated separately for events in which the probe muon originated from a  $B^0$  or a  $B_s^0$ : this allows to individually obtain  $\chi_d$  and  $\chi_s$ . The results are reported in Tab:8.

bin $p_{t,jet}$ (GeV)	$\chi_d$	$\chi_s$
10.0 - 13.0	$0.171 \pm 0.003$	$0.501 \pm 0.008$
13.0 - 16.3	$0.175 \pm 0.003$	$0.493 \pm 0.009$
16.3 - 20.4	$0.181 \pm 0.003$	$0.482 \pm 0.009$
20.4 - 26.1	$0.180 \pm 0.003$	$0.494 \pm 0.010$
26.1 - 33.8	$0.181 \pm 0.004$	$0.495 \pm 0.011$
33.8 - 48.5	$0.174 \pm 0.004$	$0.485 \pm 0.012$
48.5 - 900	$0.171 \pm 0.006$	$0.482 \pm 0.017$
10.0 - 900	$0.176 \pm 0.001$	$0.492 \pm 0.004$

Table 8:  $\chi_d$  and  $\chi_s$  estimates in  $p_{t,jet}$  bins, for MC muons deriving from a  $B^0$  and a  $B_s^0$ .

## 4.5 Analysis method

The value of  $\bar{\chi}$  is computed from the numbers of same charge and opposite charge muons coming *directly* from the the b quark that was produced in pair with the related quark that hadronized into a  $B^+$ . So, we need to separate **direct** muons from muons that derive from any other possible source, i.e. **background** muons, and this is achieved with the definition of a multivariate discriminator in the next section.

However, an additional selection is needed to separate muons that derive from the quark emitted in pairs with the one of the tag side, or **correlated** muons, from all the **uncorrelated** ones. This distinction is needed to account for double-gluon-splitting events, further analyzed in Sect:4.5.3.

A summary of these categories is reported in Tab:9.

	correlated	uncorrelated
<b>direct</b>	<ul style="list-style-type: none"> <li>• Muons emitted in the process <math>b \rightarrow \mu</math>, where <math>b</math> is the quark emitted in pairs with the one of the tag side.</li> </ul>	<ul style="list-style-type: none"> <li>• Muons emitted in the process <math>b \rightarrow \mu</math>, where <math>b</math> is a quark unrelated to the one in the tag side, as in DGS events.</li> </ul>
<b>background</b>	<ul style="list-style-type: none"> <li>• Muons emitted in the process <math>b \rightarrow X \rightarrow \mu</math>, where <math>b</math> is the quark emitted in pairs with the one of the tag side.</li> </ul>	<ul style="list-style-type: none"> <li>• Muons emitted in the process <math>b \rightarrow X \rightarrow \mu</math>, where <math>b</math> is a quark unrelated to the one in the tag side</li> <li>• muons not emitted from a b quark</li> <li>• pile-up muons</li> </ul>

Table 9: Distinction of direct-background and correlated-uncorrelated muons.

Taking all this into account, we can now rewrite Eq:3 as follows:

$$\bar{\chi} = \frac{\mathcal{N}(\tilde{\mu}_{SC})}{\mathcal{N}(\tilde{\mu}_{OC}) + \mathcal{N}(\tilde{\mu}_{SC})}$$

where  $\tilde{\mu}$  can be identified as **correlated direct muons**.

### 4.5.1 Direct and background muons

In order to separate between "direct" muons and "background" ones, a multivariate discriminator " $\Psi$ " was developed in a previous work [28] with machine learning techniques (see Appendix C).

In the development of the discriminator, the following variables are used:

- $p_T$  (*PtMuPrb*): transverse momentum of the probe muon.
- $\eta$  (*EtaMuPrb*): pseudorapidity of the probe muon.
- $hTag$  (*TagMuPrb*): multivariate discriminator that separates the background from hadronic particles, defined in the previous section.
- $\mu Iso$  (*PfIMuPrb*): isolation, quantifies the total  $p_T$  of the particles emitted around the direction of the muon. It is defined as

$$\mu Iso = \frac{1}{p_T} \left( \sum_{had^\pm} p_T^{had^\pm} + \sum_{\gamma} p_T^{\gamma} + \sum_{had^0} p_T^{had^0} \right)$$

where the sums run over the charged hadrons ( $had^\pm$ ), photons ( $\gamma$ ), and neutral hadrons ( $had^0$ ) with a distance  $\Delta R$  to the lepton smaller than 0.3 .

- $\mu IsoCh$  (*ChiMuPrb*): isolation calculated considering only charged tracks.

When a jet is associated to the muon (Jet events), the following additional variables are added in the definition of  $\Psi$ :

- $p_{t,Jet}$  (*PtJet*): transverse momentum of the jet.
- $P_{tr}$ : ratio between  $p_T$  and  $p_{t,Jet}$ .
- $P_{to}$ : projection of the momentum of the muon in the direction orthogonal to that of the residual jet, computed by removing the muon from the jet.
- $\Delta R_{in}$  (*dri*): angular distance between the muon and the jet.
- $\Delta R_{out}$  (*dro*): angular distance between the muon and the residual jet.
- $Q_m Q_j$ : product of the charge of the muon with that of the residual jet.
- $m_J$  (*jetmass*): total mass of the jet.

The distributions for all the aforementioned variables for MC events are shown, in Fig:13 the variables defined for muons, in Fig:14 the ones related to the jet. The contributions of direct muons, indirect muons from b, from c and from other sources are shown separately. The reason for selecting only Jet events is now clear, since for them a larger set of variables is available to describe the event: this guarantees a better separation and improves the discriminator performance.

It should be noted that, to increase the sensitivity of the analysis and reduce model-dependent systematic uncertainties, the training and validation of the discriminator has been performed independently in seven bin of  $p_{T,jet}$  (see below). For the sake of simplicity, only the overall distributions are shown here.

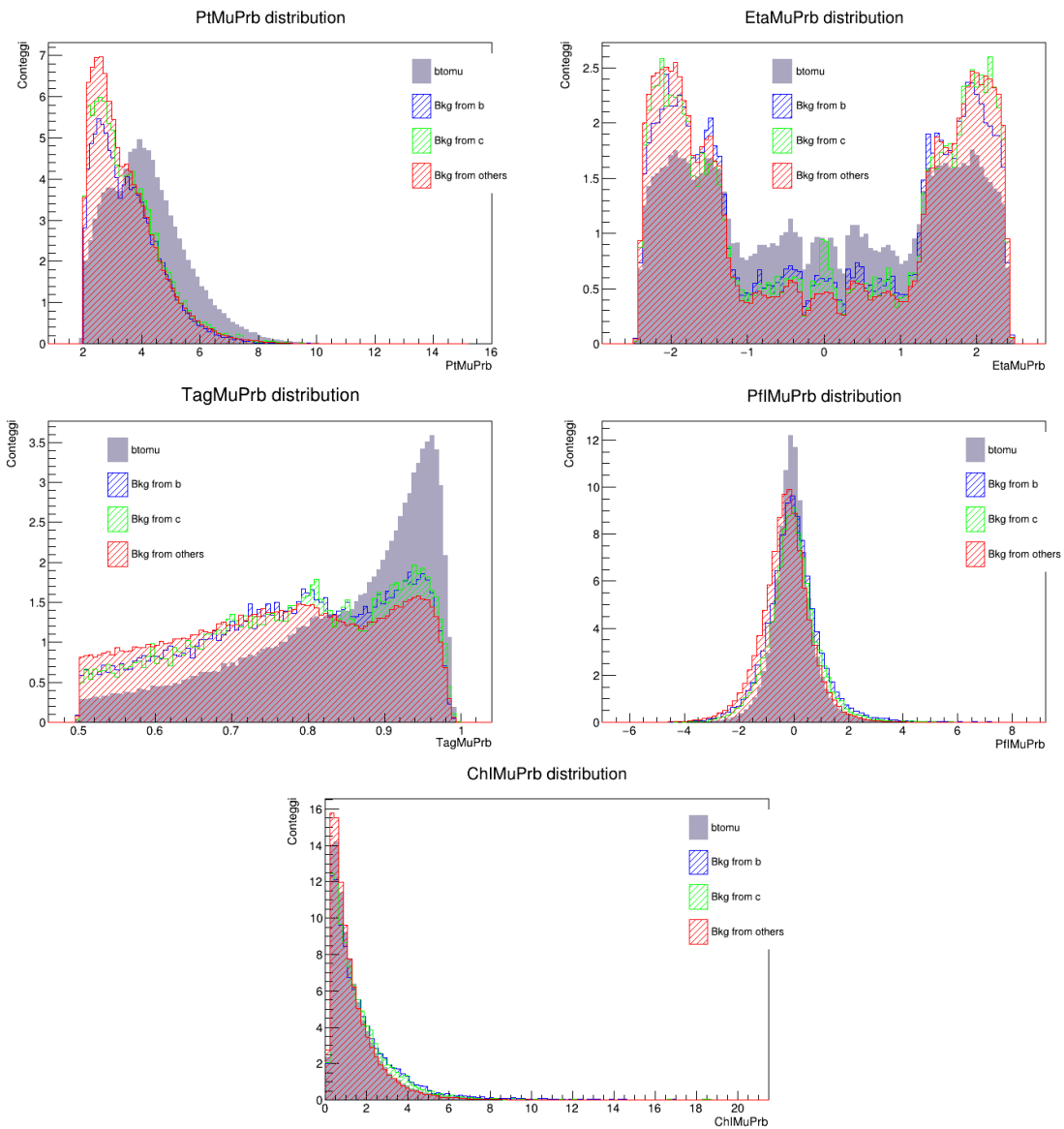


Figure 13: Distributions for all the variables defined for each probe muon; the contributions of direct muons, muons from b, from c and from other sources are shown separately.

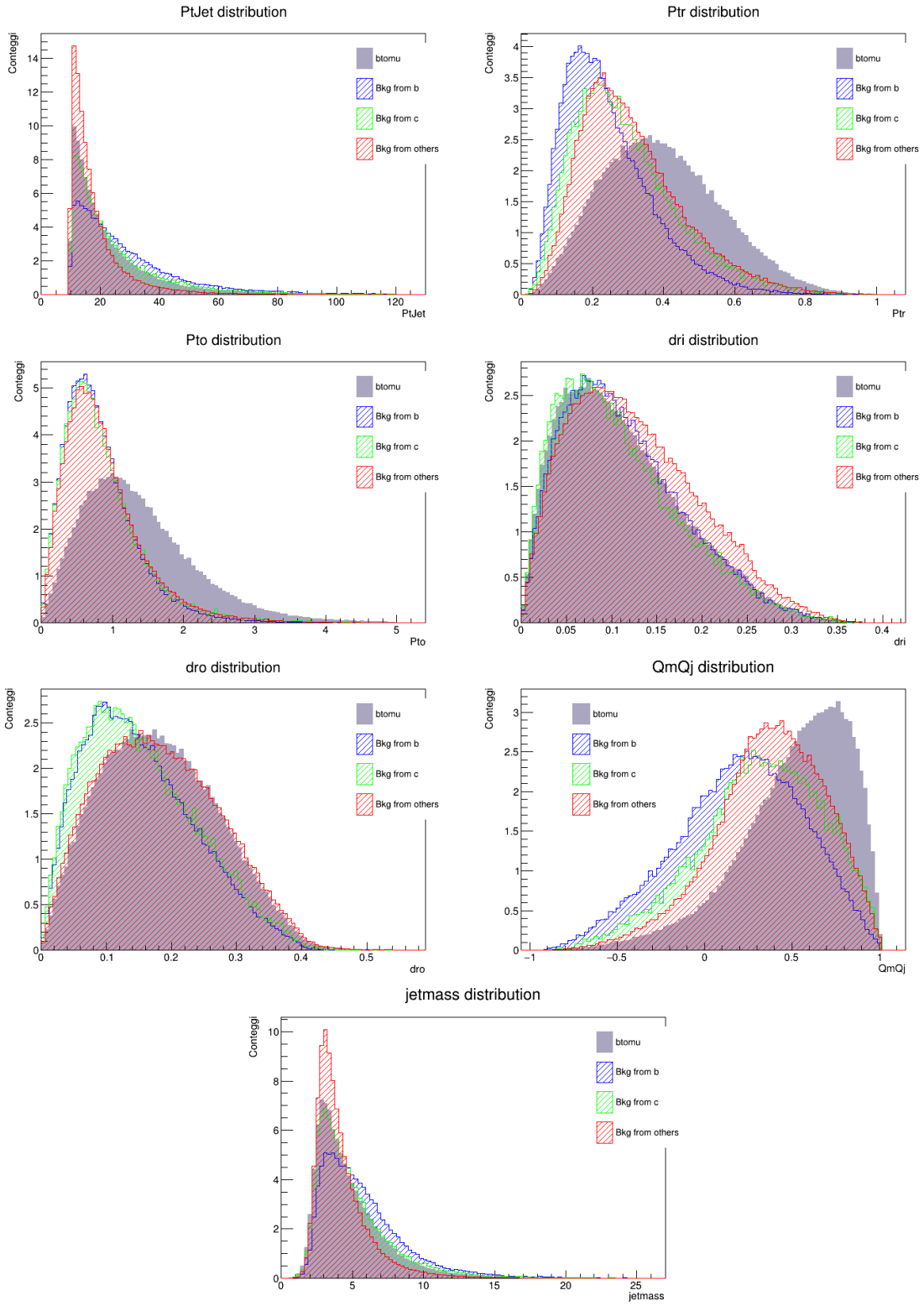


Figure 14: Distributions for all the variables defined for each reconstructed jet; the contributions of direct muons, muons from b, from c and from other sources are shown separately.

A preliminary fit on the multivariate discriminator  $\Psi$  is performed, in order to assess the agreement of the simulation with the data. The results of this check are not used for the extraction of  $\bar{\chi}$ . The fits are performed after side-band-subtracting the contributions of the background in the tag side, as explained in detail in section 4.6

The fit is performed in seven bins of  $p_{t,Jet}$ . This choice:

- improves the separation between signal and backgrounds;
- reduces the sensitivity to the mechanisms of production and fragmentation of b-quarks;
- ... and therefore improves the agreement between the fit results and the data
- provides a test of the dependence of  $\bar{\chi}$  on the B hadron  $p_T$ , for which we use  $p_{t,Jet}$  as a proxy.

The bins edges are: (10.0, 13.0, 16.3, 20.4, 26.1, 33.8, 48.5, 900) GeV.

This division ensures that the bins are equally populated, with statistics large enough to avoid sizable fluctuations.

Since for the distribution of  $\Psi$  there is no obvious analytical representation, the corresponding MC distributions are exploited to define template functions, one for the "direct" and one for the "background" category in each bin, as models to be fitted to the data.

Results of the preliminary  $\Psi$  fit are shown in Fig:15 for All-Charge Jet events (ACJet). The fit is sensitive to the contribution of direct muons, with distributions that are well separated from the background ones. Furthermore, the distribution of  $\Psi$  in the data is well reproduced by the fitting functions from the simulation. However, for some bins the normalized residues show a systematic behavior at high values of  $\Psi$ ; this effect should be further analyzed.

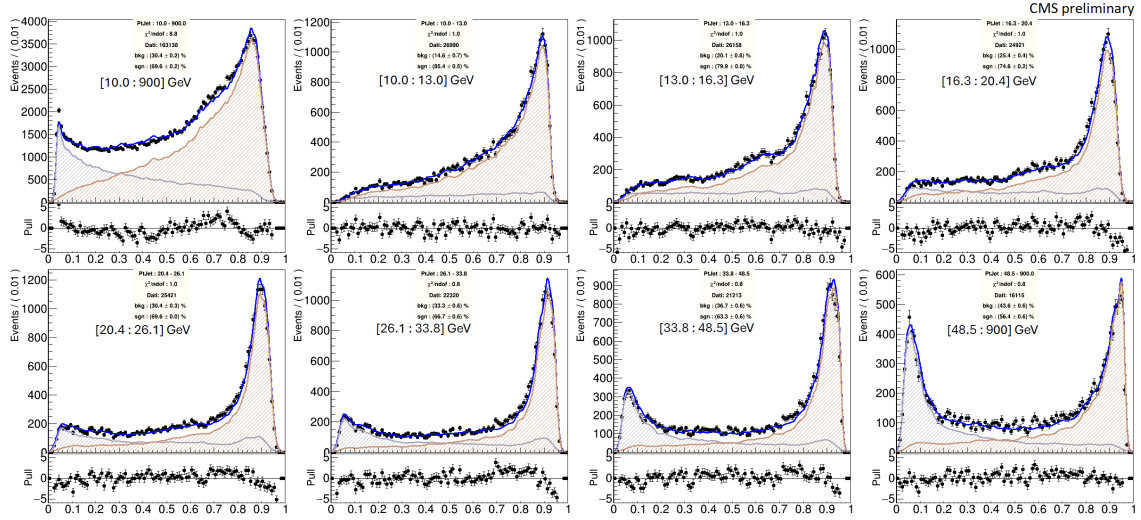


Figure 15: Fit on  $\Psi$  for ACJet events in bins of  $p_{T,jet}$ . The first bin, top-left, extends in the full  $p_T$  range [10 : 900] GeV. The panels on the bottom show the pull of the fit, bin by bin, defined as the difference from the data and the fit results divided by the statistical error on the data.

#### 4.5.2 Correlated and uncorrelated muons

In this section, we want to achieve a good separation between correlated muons, emitted by the b quark associated with the  $B_{tag}$ , and uncorrelated ones.

Separating correlated from uncorrelated events is necessary to subtract the background from direct muons produced by double gluon splitting (see next section 4.5.3) without resorting to models. This also increases the sensitivity of the fit, because it further separates uncorrelated events (pile-up, muons from  $c\bar{c}$ , from hadrons or light resonances).

The following variables are computed for each muon in the probe side, to check if they could be used to discriminate the correlated ones.

- $\Delta\phi = \phi(B_{tag}) - \phi(\mu)$
- $\Delta\eta = \eta(B_{tag}) - \eta(\mu)$

The distributions are visible in Fig:16 for  $\Delta\eta$  and in Fig:17 for  $\Delta\phi$ : correlated events on the left panels, uncorrelated on the right.

The distributions of  $\Delta\eta$  are well consistent among the same sets of events: correlated events show a sharper-almost gaussian shape, while uncorrelated events reveal a broader peak.

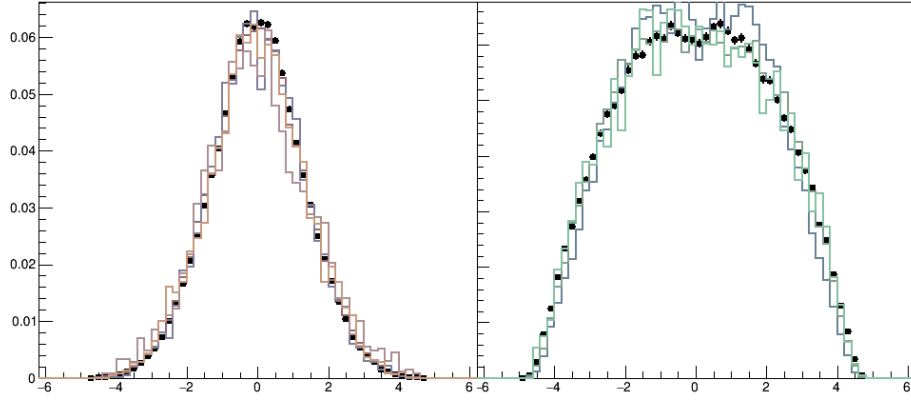


Figure 16:  $\Delta\eta$  distributions are presented: on the left panel correlated events are shown, points with error bars represent direct muons while the other histograms represent the distribution of the correlated background sources; on the right panel uncorrelated events, points with error bars represent pile-up events, while the histograms represent all the other uncorrelated sources.

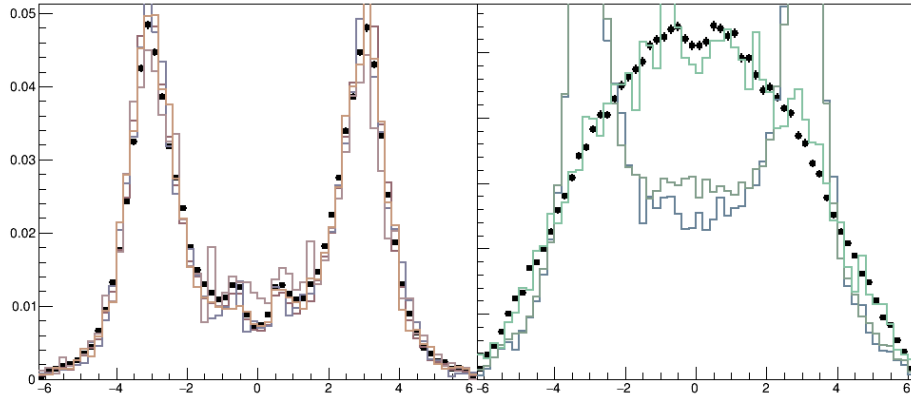


Figure 17:  $\Delta\phi$  distributions are presented: on the left panel correlated events are shown, points with error bars represent direct muons while the other histograms represent the distribution of the correlated background sources; on the right panel uncorrelated events, points with error bars represent pile-up events, while the histograms represent all the other uncorrelated sources.

In contrast, it is more difficult to interpret the  $\Delta\phi$  distributions: while the shapes for the correlated events are well consistent, that is not the case for uncorrelated events, as they are different case by case. For example, fake hadrons and the  $c\bar{c}$  distributions are closer to those of the signal.

Another problem that affects  $\Delta\phi$  is that the distributions in the data are not well represented by the simulation. In Fig:18 the two contributions are shown, separately for non pile-up and pile-up events. It is evident that, for pile-up-depleted events, the peak width is not coherent. Interestingly, the pile-up case is reproduced correctly instead, but these events are not used in the signal extraction.

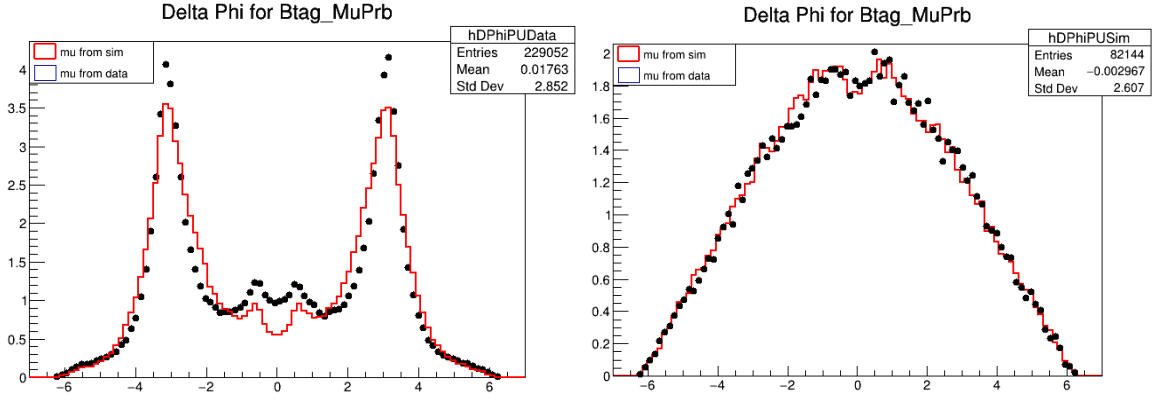


Figure 18: Comparison of  $\Delta\phi$  in the data (points with error bars) and in the simulation. On the left panel, PU-depleted events; on the right the same for PU events.

For these reasons, we only consider the variable  $\Delta\eta$  to discriminate the uncorrelated contribution from the correlated.

As in the previous case, no analytical distributions are assumed to represent the shapes of the  $\Delta\eta$  variables, so MC events are used to define the corresponding template functions, which are then fitted to the data. Different categories of muons from the simulation can be used to describe uncorrelated events and to produce template functions, as all the muons that do not derive from a b quark or pile-up muons: we assume that the uncorrelated distribution is represented by muons from the charm, from  $\pi$  or  $K$  and from other sources. The template functions for correlated events derive from both direct muons and other correlated sources.

A preliminary fit on  $\Delta\eta$  is performed on ACJet events of the dataset, keeping the same binning used in the  $\Psi$  fit. The results are shown in Fig:19. In this case too, the overall distribution of  $\Delta\eta$  in the data is well reproduced by the simulation, even if the data points are systematically lower close to the peak.

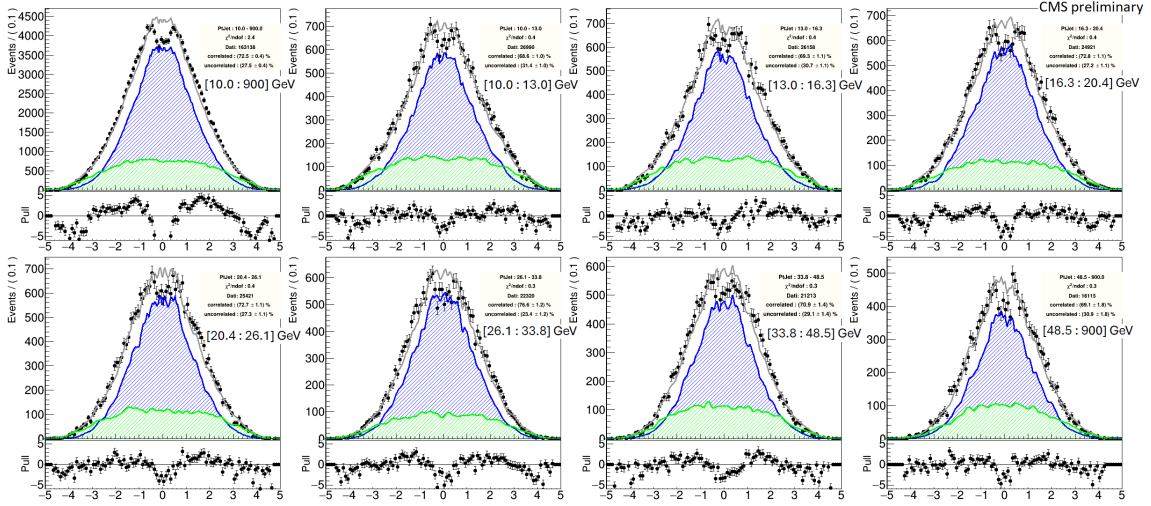


Figure 19:  $\Delta\eta$  fit on ACJet events in bins of  $p_{T,jet}$ . The first bin, top-left, extends in the full  $p_T$  range [10 : 900] GeV.

### 4.5.3 A simulation study of DGS events

A particular type of uncorrelated background consists of double-gluon-splitting (DGS), events of the type  $pp \rightarrow b\bar{b}b\bar{b}X$ , in which four (rarely even six) weakly decaying B hadrons are produced. The number of events of the simulation in which two, four, or six B hadrons are generated is listed in Tab:10. The simulation allows for the correct association of the muon with the parent B-hadron, but there is not enough information to assess whether this last is correlated or not with the  $B_{tag}$  in the case of four (or more) B hadrons.

# generated B hadrons	2	4	6
# events	245140	15140	574

Table 10: Number of simulated events with 2, 4 or 6 generated B hadrons.

For this reason, and as a test of our approach to disentangle correlated from uncorrelated muons, we compute on a statistical basis the contribution of correlated and uncorrelated direct muons by performing a fit on the  $\Delta\eta$  distributions of simulated events with four gen-

erated long-lived B-hadrons, using the templates obtained from events with two B hadrons shown in the previous paragraph.

To do that, direct muons are separated according to their charge, Fig:20-21, and also depending on the type of B meson from which they originate, either  $B^0$ ,  $B^+$  or  $B_s^0$  in Fig:22-23-24 (muons from the corresponding anti-mesons are also included). An additional separation between OC and SC is present within each sub-sample.

In Tab:11 the relative contributions and the total number of correlated and uncorrelated muons are shown for each subsample.

In all cases, the number of correlated muons present in the SC sub-sample is smaller than in the OC case; this is because the proper direct contribution is very suppressed, being only the oscillated one.

We expect the number of uncorrelated muons for the OC and SC case to be equal in each subsample because, by definition, they should not show a charge correlation. This is correctly reproduced, since looking at the result of the fit for  $\mu^+$  ( $\mu^-$ ) the difference " $Uncorrelated_{OC} - Uncorrelated_{SC}$ " is compatible with zero within  $2\sigma$  ( $< 1\sigma$ ).

Considering now the correlated muons, for the  $B^+$  case we expect the number of  $Correlated_{SC}$  to be equal to zero, as this charged state cannot oscillate. The result is equal to zero within  $2\sigma$ .

For neutral mesons, the mixing frequencies can be calculated from the numbers of  $Correlated_{SC}$  and  $Correlated_{OC}$  and they should reproduce those found in the MC. The values found from the fit are  $0.195 \pm 0.006$  for the  $B^0$ ,  $3\sigma$  far from 0.176, and  $0.425 \pm 0.005$  for the  $B_s^0$ , also more than  $3\sigma$  apart from 0.492 .

This shows that the understanding of this particular sample of events is not yet perfect.

Category	# events	Correlated (%)	Uncorrelated (%)	# Correlated	# Uncorrelated
$\mu^+$ OC	3943	$63.2 \pm 2.8$	$36.9 \pm 2.8$	$2490 \pm 109$	$1454 \pm 109$
$\mu^+$ SC	2209	$21.8 \pm 4.0$	$78.2 \pm 4.0$	$482 \pm 88$	$1728 \pm 88$
$\mu^-$ OC	3976	$60.6 \pm 2.7$	$39.4 \pm 2.7$	$2408 \pm 109$	$1568 \pm 109$
$\mu^-$ SC	2170	$24.6 \pm 4.1$	$75.4 \pm 4.1$	$535 \pm 88$	$1637 \pm 88$
from $B^0$ , OC	4079	$56.9 \pm 2.8$	$43.1 \pm 2.8$	$2321 \pm 112$	$1759 \pm 112$
from $B^0$ , SC	2370	$23.8 \pm 3.8$	$76.2 \pm 3.8$	$564 \pm 91$	$1807 \pm 91$
from $B^+$ , OC	2810	$69.2 \pm 3.2$	$30.8 \pm 3.2$	$1946 \pm 89$	$865 \pm 89$
from $B^+$ , SC	1243	$9.5 \pm 5.6$	$90.6 \pm 5.6$	$118 \pm 69$	$1125 \pm 69$
from $B_s^0$ , OC	701	$64.8 \pm 6.5$	$35.3 \pm 6.5$	$454 \pm 46$	$248 \pm 46$
from $B_s^0$ , SC	632	$53.0 \pm 6.9$	$47.2 \pm 6.9$	$335 \pm 44$	$298 \pm 44$

Table 11: Relative contributions and number of correlated and uncorrelated muons from  $\Delta\eta$  fit on different sub-samples.

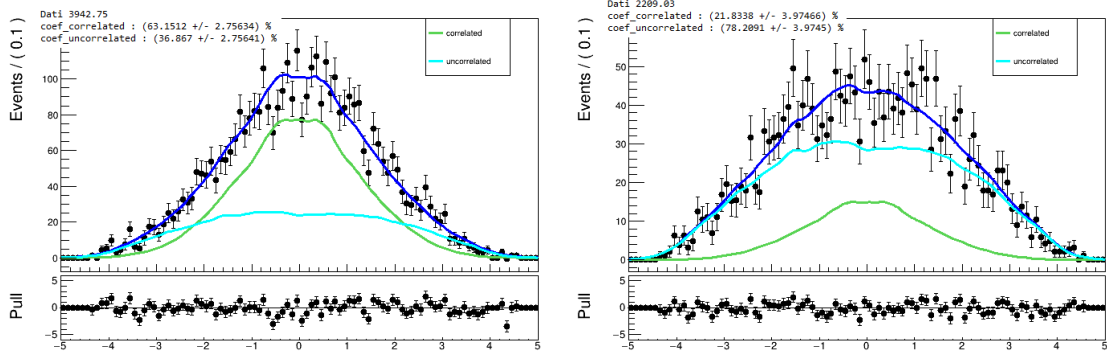


Figure 20: Fit of  $\Delta\eta$  distributions for positive direct muons, OC (left) and SC (right). The correlated and uncorrelated contributions are shown.

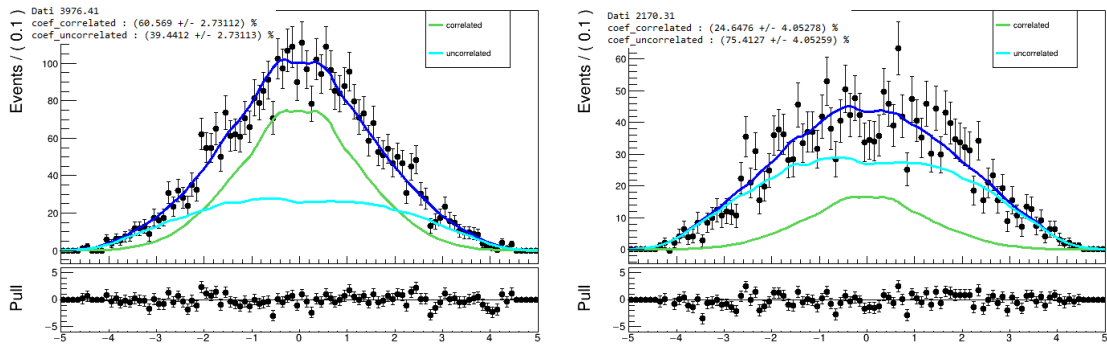


Figure 21: Fit of  $\Delta\eta$  distributions for negative direct muons, OC (left) and SC (right). The correlated and uncorrelated contributions are shown.

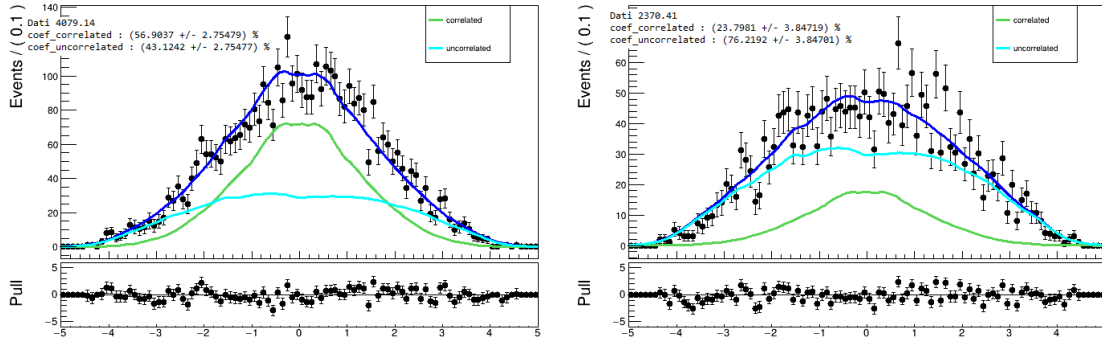


Figure 22: Fit of  $\Delta\eta$  distributions for direct muons from a  $B^0$ , OC (left) and SC (right). The correlated and uncorrelated contributions are shown.

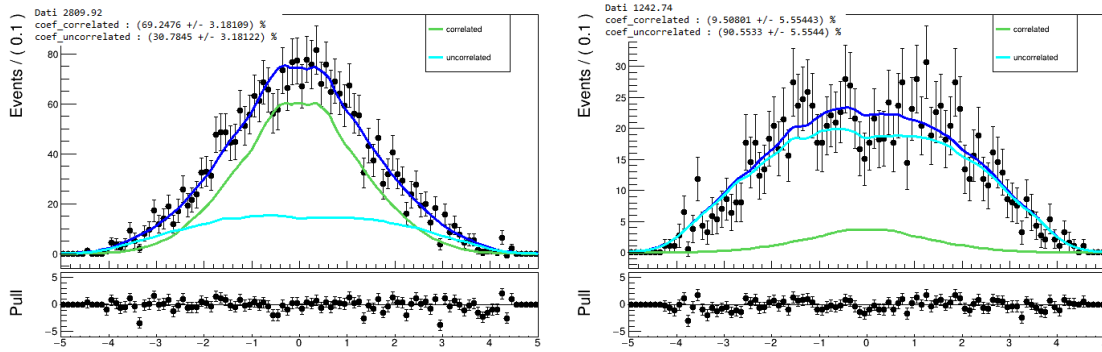


Figure 23: Fit of  $\Delta\eta$  distributions for direct muons from a  $B^+$ , OC (left) and SC (right). The correlated and uncorrelated contributions are shown.

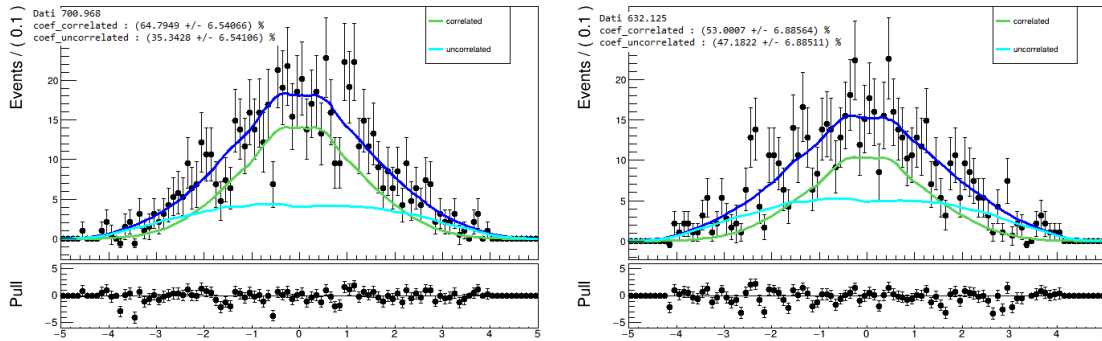


Figure 24: Fit of  $\Delta\eta$  distributions for direct muons from a  $B_s^0$ , OC (left) and SC (right). The correlated and uncorrelated contributions are shown.

## 4.6 Fitting procedure

At this point of the work, to avoid biasing the analysis by optimizing the final estimate based on some prior knowledge, the data sample is altered to blind the value of the mixing parameter. This is done by removing an unknown fraction of data, from 0% to 20%, from the dataset, for either OC or SC events. Which sample is modified is also unknown. This allows to check the quality of the fits without knowing the value of  $\bar{\chi}$ . After all the systematic uncertainties have been computed and the consistency check performed, the fit will be repeated without removal of data to extract the actual value of  $\bar{\chi}$ .

In order to extract the number of correlated direct muons in each bin of  $p_{T,jet}$ , two-dimensional fits are performed for OC and SC events separately, using the tools provided by the RooFit package; this method simultaneously considers the mass of the reconstructed tag vertex  $m_V$  and the variables  $\Delta\eta$  and  $\Psi$ .

From the simulation a template Pdf ' $H_i$ ' is created for each category that enters the fit; the weighted sum of all Pdf templates  $H_i$ ,  $H_{tot} = c_1 H_1 + \dots + c_n H_n$ , is the function used to fit the data, with the coefficients  $c_i$  being the fitting parameters. These parameters  $c_i$  are related to the relative fraction of events for each category in the data sample.

Along the mass direction, a central region ( $m_V \subseteq [5.2 : 5.34]$  GeV) and lateral regions (elsewhere) are defined. The signal Pdf that describes the resonance around the mass  $m_B$  is a *Johnson SU* distribution [1]. This Pdf results from transforming a normally distributed variable to this form:

$$z = \gamma + \delta \sinh^{-1} \left( \frac{x - \mu}{\lambda} \right)$$

The resulting Pdf is

$$\text{Pdf}_{(\gamma,\delta,\lambda,\mu)}(x) = \frac{\delta}{\lambda\sqrt{2\pi}} \frac{1}{\sqrt{1 + \left(\frac{x-\mu}{\lambda}\right)^2}} \exp \left[ -\frac{1}{2} \left( \gamma + \delta \sinh^{-1} \left( \frac{x - \mu}{\lambda} \right) \right)^2 \right]$$

and it is often used to fit mass distributions for particle decays, with the variable  $x$  representing the mass in this implementation.

The background Pdf, instead, is built combining an exponential distribution, to account for the combinatorial background, and an Erf function, to describe only partially reconstructed events (like, for instance,  $B \rightarrow K^* J/\Psi$ ,  $K^* \rightarrow K\pi$  and either the kaon or the pion is missed).

In the central and lateral regions, the signal and background Pdfs are fitted to the data points, as shown in Fig.25. The Pdfs integrals in the central and lateral regions are used to calculate the weight to assign to each point, calculated so that the only residual contribution in the central region is the one of the signal. The reweighting of the points is done with the underlying assumption that the variables  $m_V$ ,  $\Delta\eta$  and  $\Psi$  are not correlated.

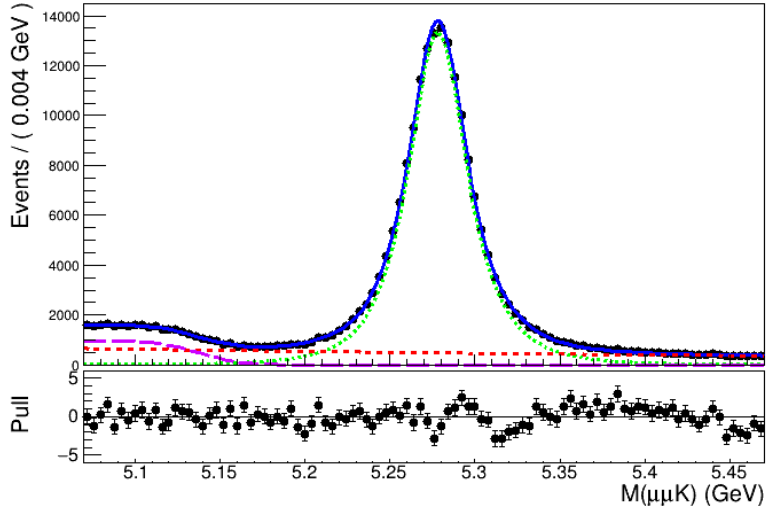


Figure 25: Fit of the vertex mass  $m_V$  distribution, for ACJet events.

After reweighing the points, the two Pdfs defined for the  $\Psi$  variable ("direct" and "background") are multiplied by the ones defined for the  $\Delta\eta$  variable ("correlated" and "uncorrelated"), to give four two-dimensional Pdfs that represent all the possible combinations of these categories.

From the fit we obtain the number of correlated direct muons for the OC and SC case, and from them we compute  $\bar{\chi}$  in each bin.

## 4.7 Check on MC

To check the consistency of the fitting procedure, we need to verify that the simulated fractions of muons in each category have been assigned correctly. This is done by dividing the MC sample into two parts. The first half is used to define the  $\Psi$  discriminator and the template functions, while the second half is treated as a dataset.

The fractions from the fit are shown in Fig.:26-27 for OC and SC events, respectively. The important result is that the direct correlated contribution percentages are as expected from the MC for each bin and for both OC and SC events, demonstrating the consistency of the fitting procedure. Furthermore, the uncorrelated direct percentages are always compatible with zero, as expected, since we removed DGS events for this test, which is the only contribution that can populate this category. The two background contributions are also correctly represented.

The same check is also performed including DGS events, and this time the expected fraction of uncorrelated direct muons is expected to be different from zero.

The results are shown in Tab:12.

The distinction between correlated and uncorrelated direct muons in the calculation of the MC percentages is obtained using the results of the fits performed on DGS events in Sect:4.5.3. For background events, instead, correlated and uncorrelated contributions are considered together.

Again, the direct correlated contribution percentages are as expected from the MC. The percentages for the other categories are also in agreement, except for direct uncorrelated events of the OC case, which are overestimated in the fit results. However, this is not expected to influence the estimate of  $\bar{\chi}$ , since it is only sensitive to direct correlated muons.

	OC			SC		
	DirCorr	DirUncorr	Bkg	DirCorr	DirUncorr	Bkg
Fit %	$73.4 \pm 2.0$	$9.5 \pm 2.1$	$17.2 \pm 2.6$	$32.6 \pm 2.5$	$2.4 \pm 1.4$	$65.0 \pm 5.0$
MC %	76.7	1.7	21.6	30.6	4.1	65.3

Table 12: Contribution of different categories of muons, as found in the fit and as expected from the MC.

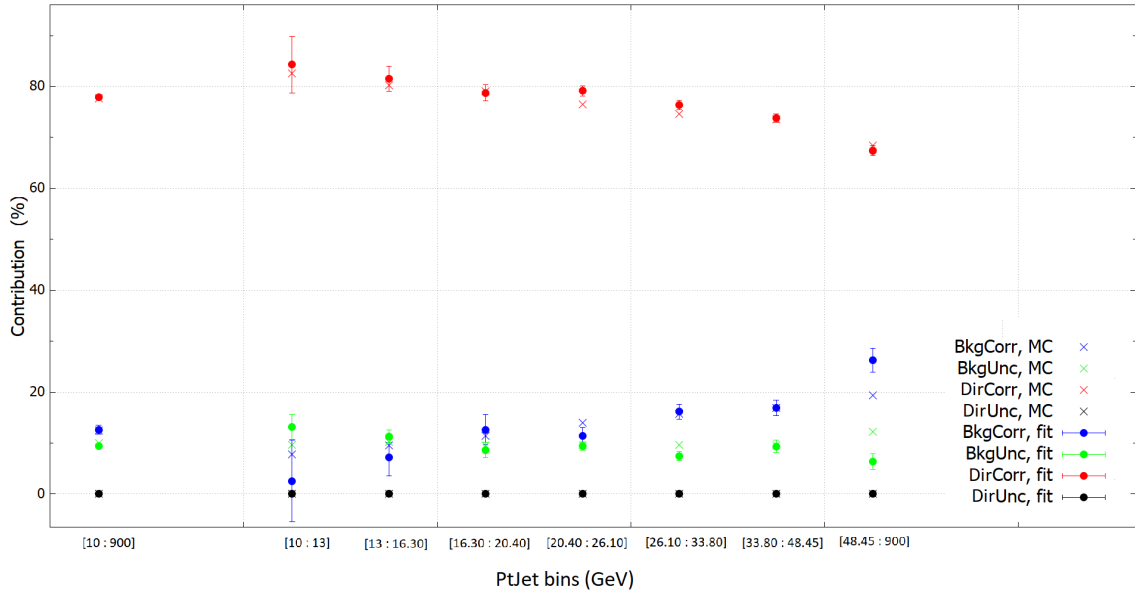


Figure 26: Comparison of the contribution of different categories, as found in the fit (points with error bars) and as expected from the MC (crosses), in  $p_{T,jet}$  bins for OC events.

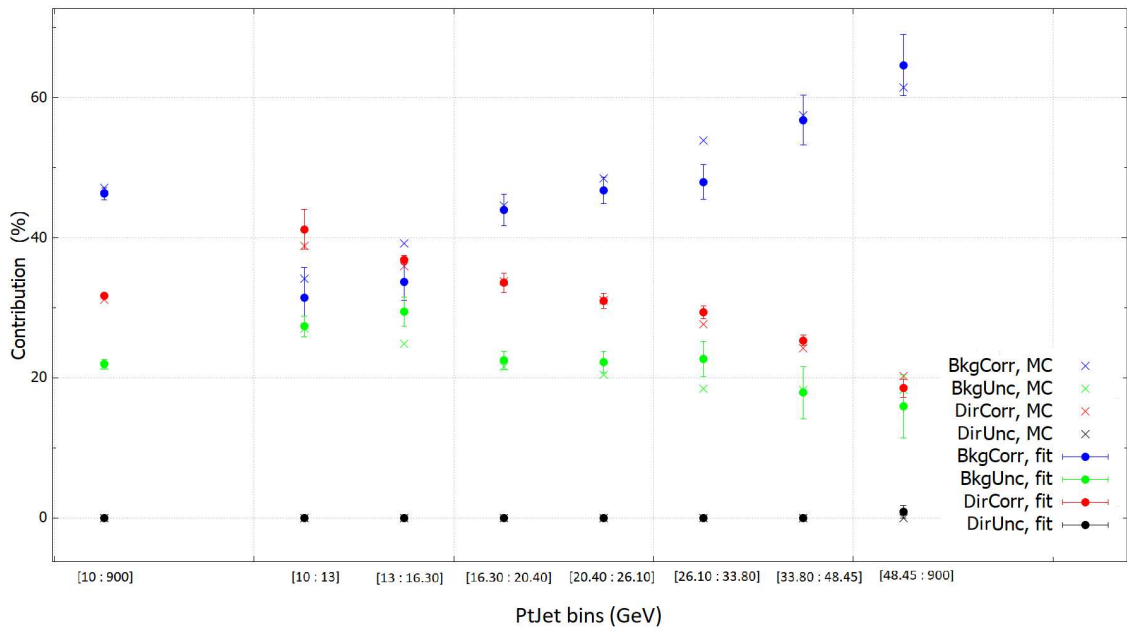


Figure 27: Comparison of the contribution of different categories, as found in the fit (points with error bars) and as expected from the MC (crosses), in  $p_{T,jet}$  bins for SC events.

## 4.8 Final fit and $\bar{\chi}$ estimate

The fit results are shown in Fig:30-31 projected along the  $\Psi$  direction, for OC and SC events respectively, and in Fig:32-33 projected along the  $\Delta\eta$  direction. In Tab:13 the numbers of correlated direct muons extracted from the fit are listed and the corresponding values of  $\bar{\chi}$  are calculated.

$p_{T,jet}$ bin	OC		SC		$\bar{\chi}$
	# events	# corr. direct $\mu$	# events	# corr. direct $\mu$	
10.0 - 13.0	20678	15341 $\pm$ 418	6331	3189 $\pm$ 347	0.172 $\pm$ 0.016
13.0 - 16.3	19728	15036 $\pm$ 397	6446	3012 $\pm$ 217	0.167 $\pm$ 0.011
16.3 - 20.4	18575	14462 $\pm$ 392	6359	2490 $\pm$ 109	0.147 $\pm$ 0.006
20.4 - 26.1	18557	13868 $\pm$ 882	6872	1971 $\pm$ 278	0.124 $\pm$ 0.017
26.1 - 33.8	15869	11613 $\pm$ 592	6457	1688 $\pm$ 249	0.127 $\pm$ 0.017
33.8 - 48.5	14525	9583 $\pm$ 637	6688	1292 $\pm$ 318	0.119 $\pm$ 0.027
48.5 - 900	10437	6535 $\pm$ 661	5668	923 $\pm$ 324	0.124 $\pm$ 0.040

Table 13: Number of correlated direct muons for OC and SC events extracted from the fit, in  $p_{T,jet}$  bins.

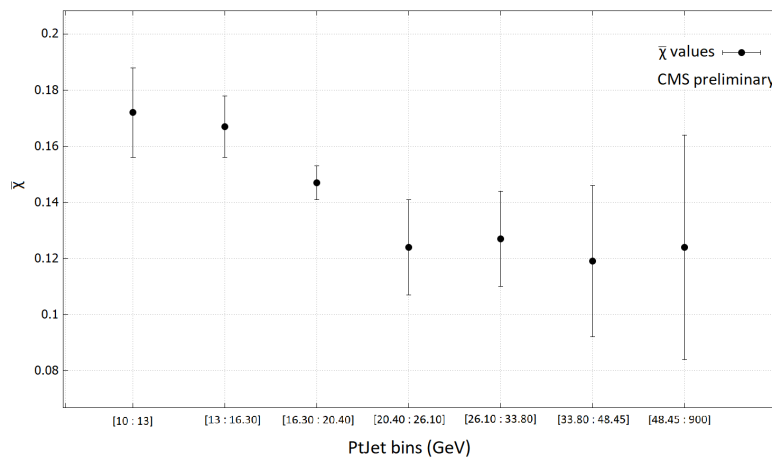


Figure 28:  $\bar{\chi}$  values in  $p_{T,jet}$  bins. The values decrease with an increasing  $p_t$ .

As the  $\bar{\chi}$  estimate has been blinded, we will not comment on the absolute values obtained from the fit. However, a clear dependence on  $p_{T,jet}$  can be observed. In particular, the values of  $\bar{\chi}$  decrease with an increasing  $p_t$ : this is consistent with the dependence observed for the ratio  $R_S$ . The statistical error could be further reduced by increasing the sample size. For example, this can be done by including the data acquired during Run3.

We also want to obtain an estimate of  $\bar{\chi}$  in the full range of  $p_T$ , but this cannot be achieved by simply considering the results of the fit in the bin [10.0 - 900] GeV. This is because, as already discussed, in the full range of momentum the variable  $\Psi$  does not properly represent muons with different  $p_T$ . This is therefore done by adding the contributions of singular bins in the range [binEdge : 900] GeV, where 'binEdge' increases from 10.0 to 48.5 , as reported in Tab:14.

As the momentum dependence is now integrated out, the values are much more flattened, as shown in Fig:29. Given the higher number of events, especially in the first integrated bins, the estimates are also more precise.

$p_{T,jet}$ bin	OC		SC		$\bar{\chi}$
	# events	# corr. direct $\mu$	# events	# corr. direct $\mu$	
10.0 - 900	118369	$86437 \pm 1567$	44821	$14565 \pm 724$	$0.144 \pm 0.007$
13.0 - 900	97691	$71096 \pm 1510$	38490	$11376 \pm 635$	$0.138 \pm 0.007$
16.3 - 900	77963	$56060 \pm 1457$	32044	$8363 \pm 597$	$0.130 \pm 0.009$
20.4 - 900	59388	$41599 \pm 1404$	25685	$5874 \pm 587$	$0.124 \pm 0.011$
26.1 - 900	40831	$27731 \pm 1092$	18813	$3903 \pm 517$	$0.123 \pm 0.015$
33.8 - 900	24962	$16118 \pm 918$	12356	$2215 \pm 454$	$0.121 \pm 0.023$
48.5 - 900	10437	$6535 \pm 661$	5668	$923 \pm 324$	$0.124 \pm 0.040$

Table 14: Number of correlated direct muons for OC and SC events extracted from the fit, in integrated bins of  $p_{T,jet}$ .

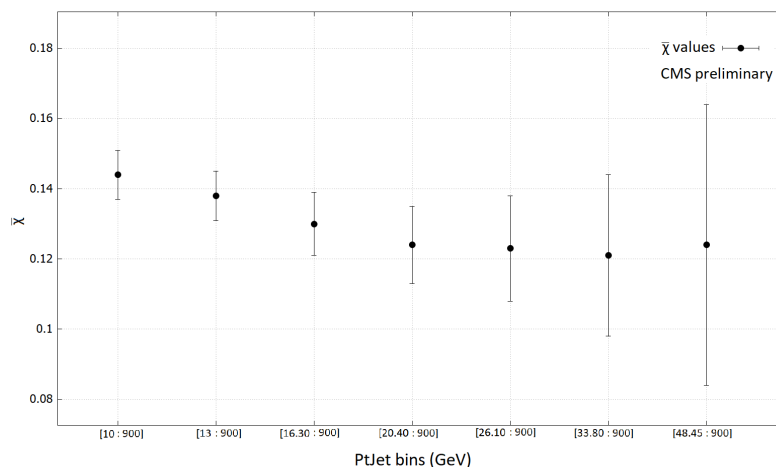


Figure 29:  $\bar{\chi}$  values in integrated bins of  $p_{T,jet}$ . The values appear more flattened.

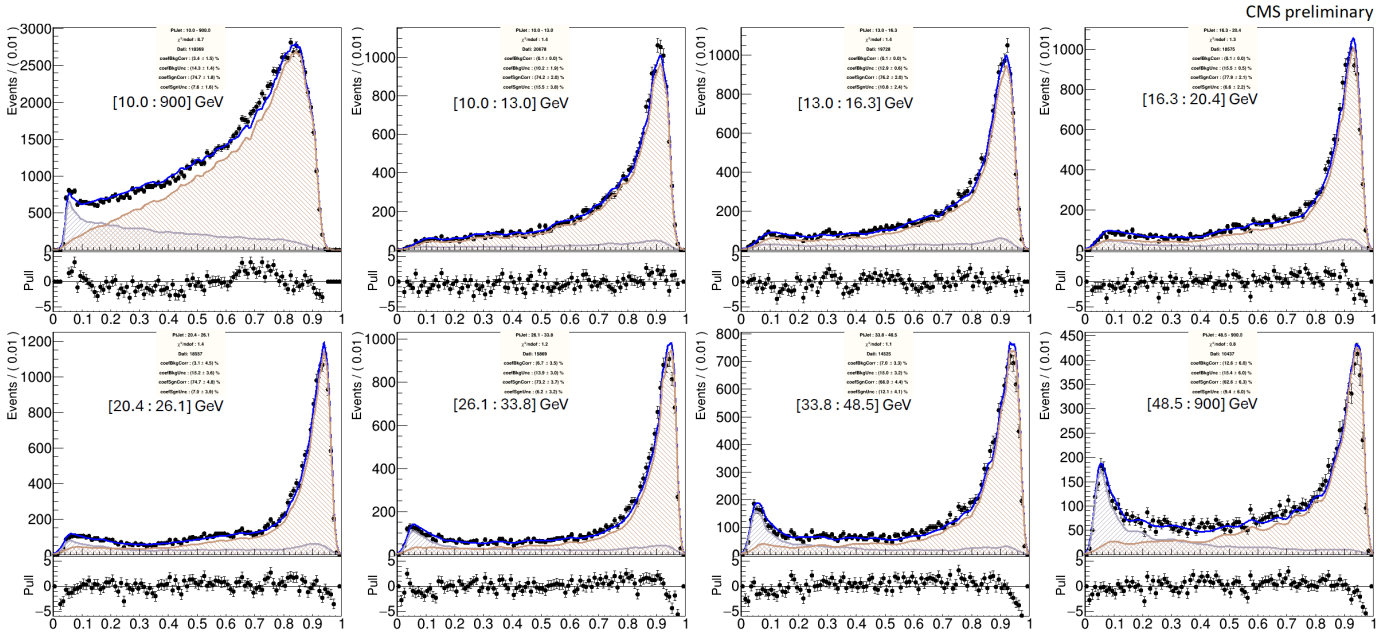


Figure 30: Result of the two-dimensional fit  $\Delta\eta$  w.r.t.  $\Psi$  in  $p_{T,jet}$  bins for OC events, projected along the  $\Psi$  direction.

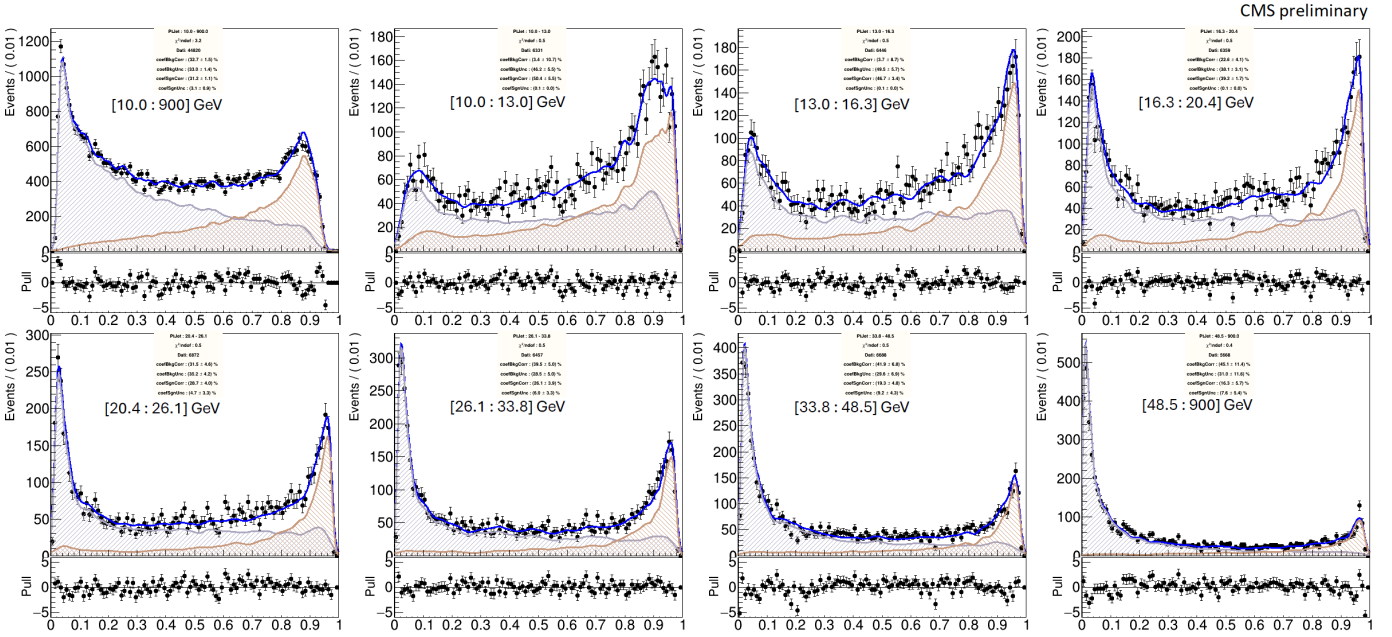


Figure 31: Result of the two-dimensional fit  $\Delta\eta$  w.r.t.  $\Psi$  in  $p_{T,jet}$  bins for SC events, projected along the  $\Psi$  direction.

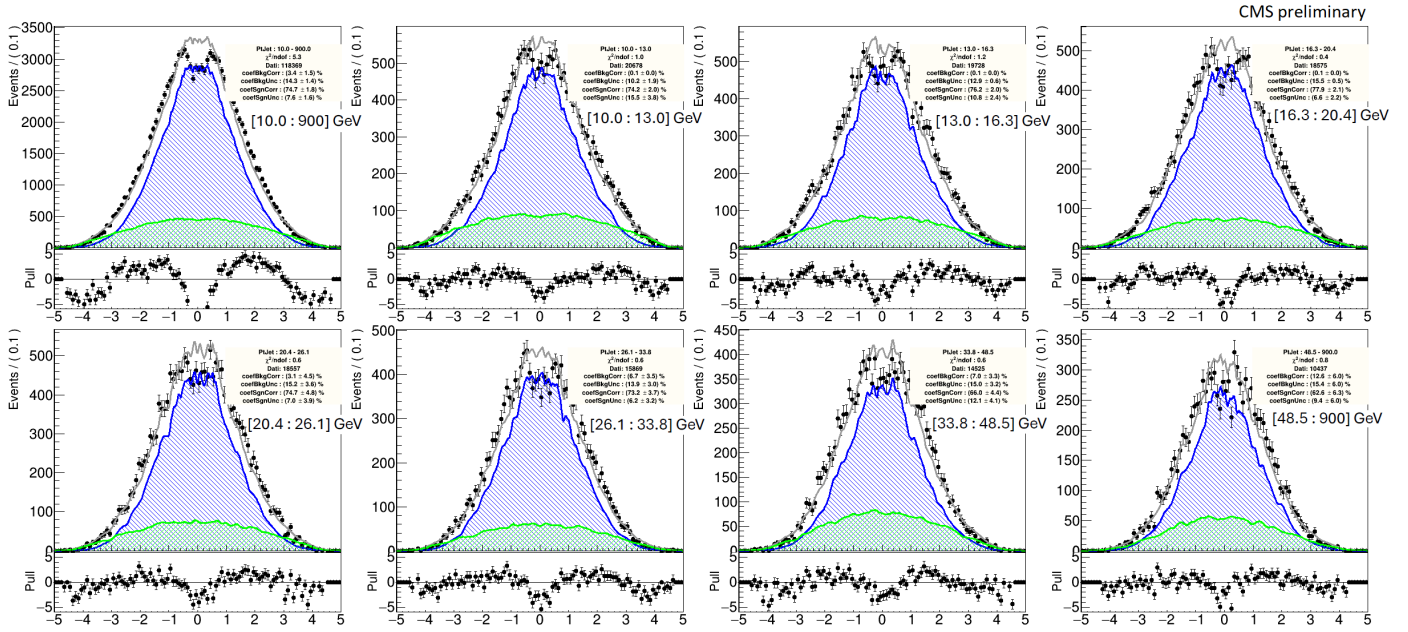


Figure 32: Result of the two-dimensional fit  $\Delta\eta$  w.r.t.  $\Psi$  in  $p_{T,jet}$  bins for OC events, projected along the  $\Delta\eta$  direction.

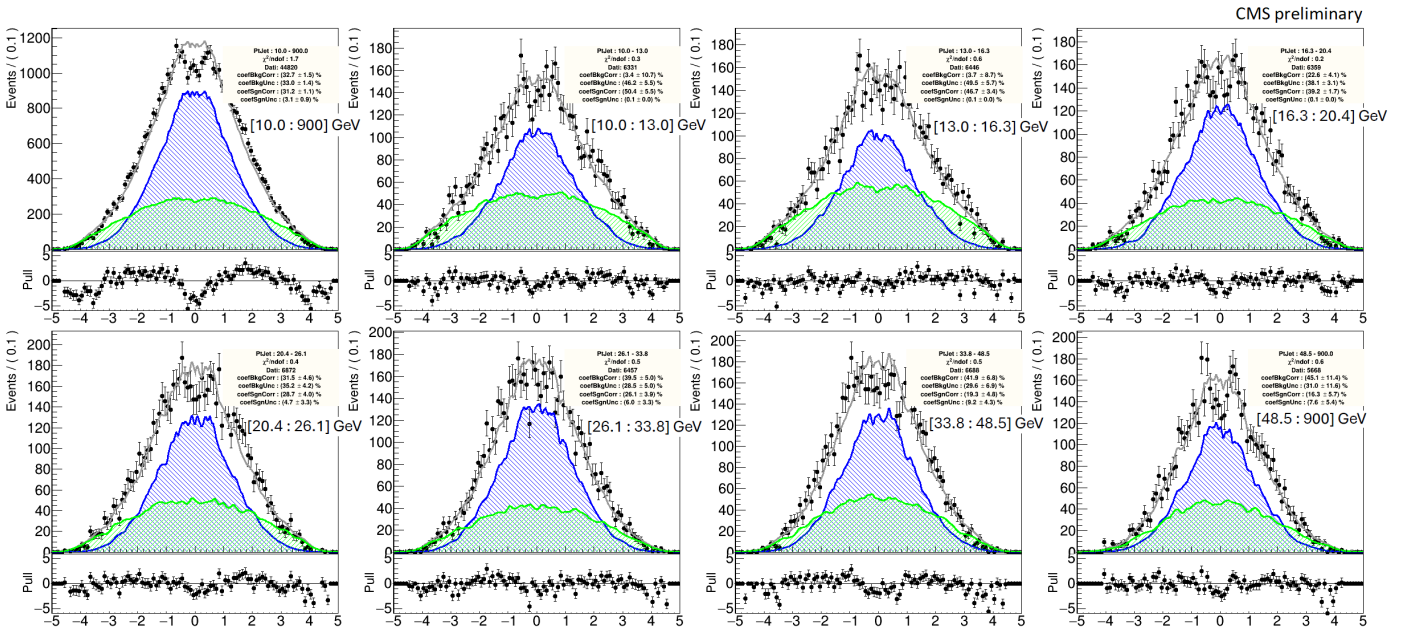


Figure 33: Result of the two-dimensional fit  $\Delta\eta$  w.r.t.  $\Psi$  in  $p_{T,jet}$  bins for SC events, projected along the  $\Delta\eta$  direction.

In order to test possible asymmetries in the production,  $\bar{\chi}$  is also computed separately for events tagged by a  $B^+$  and  $B^-$  meson. The results are shown in Fig:34. No differences between the two estimates are visible within the uncertainties that, especially for the last two bins, are quite large. This is due to a further reduction of the statistic when splitting the dataset in two.

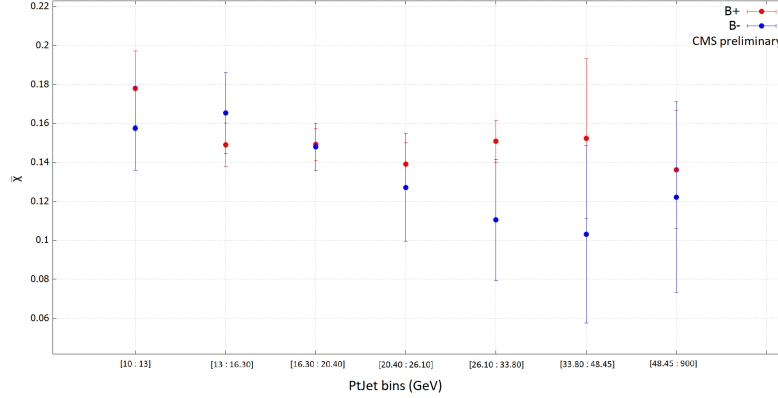


Figure 34:  $\bar{\chi}$  values in  $p_{T,jet}$  bins, calculated separately for events tagged by a  $B^+$  (in red) and  $B^-$  (in blue) meson. No differences between the two estimates are visible within the uncertainties.

The  $\bar{\chi}$  values for  $B^+$  and  $B^-$  events are also calculated in integrated bins, defined as in the previous paragraph. The results are shown in Fig:35. The values obtained from events tagged by a  $B^-$  are systematically lower, but still compatible within the uncertainties.

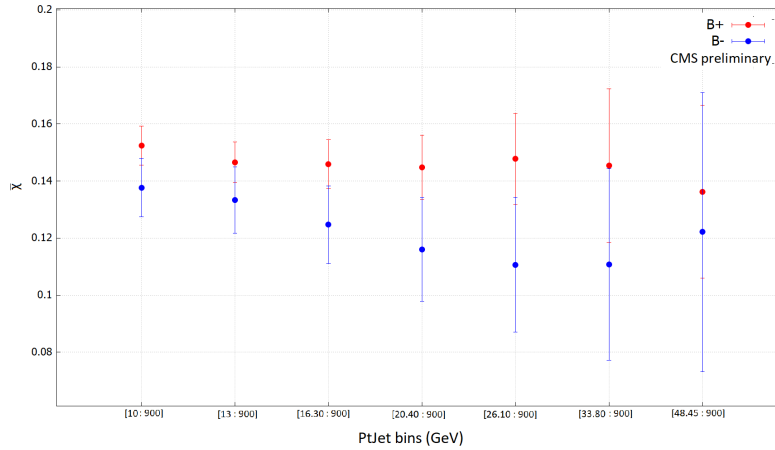


Figure 35:  $\bar{\chi}$  values integrated in  $p_{T,jet}$  bins, calculated separately for events tagged by a  $B^+$  (in red) and  $B^-$  (in blue) meson. No differences between the two estimates are visible within the uncertainties.

## 4.9 Cross check on uncorrelated muons

In Sect.4.5.2, the  $\Delta\eta$  distribution of simulated muons from the charm, from  $\pi$  or K is chosen to represent uncorrelated events. An alternative approach would have been to use the distribution from pile-up events as a template. We now want to check whether this particular choice causes a systematic deviation of the final estimate of the mixing parameter.

In Tab:15 the values of  $\bar{\chi}$  obtained from the fit with muons of the charm, from  $\pi$  or K are listed in the second column, while in the third column we show the same values from the fit with the template of pile-up muons. In the last column, the error on  $\Delta\bar{\chi}$  is calculated as the difference in quadrature of the errors of the two estimates.

The eventual systematic effect is smaller than the statistical significance of this test so, with the current statistical errors, the choice of a particular category of muons to represent the uncorrelated distribution does not affect the fit results in a sensible way. However, the use of data-driven templates, i.e. the ones from pile-up, results in more precise estimates of  $\bar{\chi}$ .

$p_{T,jet}$ bin	$\bar{\chi}_{(c, \pi, K)}$	$\bar{\chi}_{(PU)}$	$\Delta\bar{\chi}$
10.0 - 13.0	$0.172 \pm 0.016$	$0.168 \pm 0.013$	$0.004 \pm 0.009$
13.0 - 16.3	$0.167 \pm 0.011$	$0.164 \pm 0.009$	$0.003 \pm 0.006$
16.3 - 20.4	$0.147 \pm 0.006$	$0.145 \pm 0.006$	$0.002 \pm 0.003$
20.4 - 26.1	$0.124 \pm 0.017$	$0.127 \pm 0.017$	$0.003 \pm 0.003$
26.1 - 33.8	$0.127 \pm 0.017$	$0.128 \pm 0.014$	$0.001 \pm 0.010$
33.8 - 48.5	$0.119 \pm 0.027$	$0.123 \pm 0.019$	$0.004 \pm 0.019$
48.5 - 900	$0.124 \pm 0.040$	$0.124 \pm 0.041$	$0.0004 \pm 0.0113$

Table 15:  $\bar{\chi}$  values in  $p_{T,jet}$  bins obtained using different templates for uncorrelated muons. In the last column, the combination of the two estimate is shown. The values of  $\bar{\chi}_{(c, \pi, K)}$  are the ones shown in Tab:13.

## 5 Conclusions

In this work a novel method for measuring the time-integrated mixing probability is implemented, using events with a fully reconstructed  $B^+$  meson, tagging the flavor of the other  $b$  at production time, and an additional muon, providing the flavor at decay time. After selecting the events, two variables are identified to distinguish muons that decay directly from  $b$  quarks from background muons ( $\Psi$  discriminator) and to separate muons correlated in production with the  $B_{tag}$ , from uncorrelated ones ( $\Delta\eta$  between the  $B_{tag}$  and the muon in the "probe" side).

Tests are performed so as to ensure that the relevant discriminant variables for the main background sources are correctly described in the simulation.

The analysis is blinded to avoid introducing bias based on prior knowledge of the value of the mixing parameter. Then, a two-dimensional fit is performed to extract the number of correlated direct muons in each bin of transverse momentum. The mixing probability is calculated from these numbers. Through the checks on the MC, we show that the fitting procedure is consistent.

The study of systematic uncertainties has just begun. Fits with sets of parameterized ("toy") simulated events need to be performed to assess the contribution of the finite MC sample to the statistical uncertainty.

A preliminary check for the presence of production asymmetries is performed by computing the mixing parameter separately for  $B^+$  and  $B^-$  tagged events. The two values show no discrepancy within the uncertainties.

The use of MC-inspired or data-driven templates for the background  $\Delta\eta$  distribution does not change in a significant way the result, but the  $2\sigma$  deviations in the DGS MC simulation is yet to be understood.

As the measurement is performed in bins of  $p_{T,jet}$ , a small sensitivity of the result on the models assumed to define the shapes of  $\Psi$  and  $\Delta\eta$  for signal and background muon is expected. This has however to be quantified by using different models for  $b$ -production, fragmentation and decay, and for the backgrounds. The effect of adjusting the simulation to the data to correct the slight differences observed in some fits should be assessed as well. The discrepancy between the distribution of the  $\Psi$  parameter found in the fit could be treated with a smearing procedure, while the effect of the  $\Delta\eta$  uncorrelated distributions on the fit results could be investigated by looking at different production models.

Any effect of reconstruction efficiency should cancel out when computing the ratio of oscillated to total events. Because the analysis is based on a fully inclusive method, systematic effects from uncertainties in the recorded luminosity or event yields are not relevant.

After taking systematics into account, the blinding can be removed and from the final measurement of the mixing parameter a linear combination of the production fractions  $f_d$  and  $f_s$  can be derived. Furthermore, to independently obtain the values of  $f_d$  and  $f_s$ , the same analysis can be performed for two different datasets selected from different bins of the impact parameter.



## A Cascade background characterization

This appendix is devoted to the characterization of background muons originating in the process  $b \rightarrow c \rightarrow \mu^+$ , the so called "cascade decay". It is particularly important to check if this background is correctly reproduced by the simulation because, having an opposite charged correlation with the  $B_{tag}$ , these muons might be mistakenly labeled as 'oscillated events'. A dedicated control region has been defined, considering events with two muons in the probe side.

According to the classification shown in Tab:7 in the first section, a muon can be produced in 20 different processes, so there are 400 possible combinations of categories to classify two muon events. In order to reduce the number of possible combinations and gather physically related processes, we classify them by defining the following categories:

1. "Direct+cascade"    ( $b \rightarrow \mu$ ,     $b \rightarrow c \rightarrow \mu$ )
2. "DGS<sub>direct</sub>"    (two  $b \rightarrow \mu$     or     $b \rightarrow \mu$ ,  $c \rightarrow \mu$ )
3. "bb<sub>indirect</sub>"    ( $b \rightarrow c \rightarrow \mu$     or     $b \rightarrow \tau \rightarrow \mu$ )
4. "others"

In order to produce a sample of events enriched in "direct + cascade" pairs, the following conditions are applied: the two probe muons must have opposite charges, they both have to verify  $|\Delta z| = z_{prb} - z_{tag} < 0.25$  to remove the pile-up contribution (see next Section B) and the OC muon has to verify  $\Psi > 0.7$ , so that with high probability it is a direct muon.

For all these muon pairs, the invariant mass 'M<sub>inv</sub>' is calculated as  $M_{inv} = \sqrt{(p_{\mu 1} + p_{\mu 2})^2}$ , where  $p_{\mu i}$  are the quadrivectors of the two muons of the pair. Events in which the two muons come from the same b are expected to populate the region with small invariant mass, whereas events with two unrelated muons are expected to span a much wider range. In order to test the separation capability of the invariant mass for the aforementioned categories, a fit on M<sub>inv</sub> is performed as described in Sect.4.6. The range  $M_{inv} \subseteq [0 : 15]$  is selected in order to guarantee a nice resolution of the peak but also a sufficiently large tail contribution, that is more sensitive to the "DGS" and "other" categories. The fit result is shown in Fig.36 and for each category the relative fractions of events are shown in Tab.16. The overall distribution is well reproduced by the simulation, even if for the single contributions the agreement is not perfect; in particular, the percentage for "direct+cascade" is higher than predicted in the MC.

In the region  $M_{inv} \subseteq [0:3]$  GeV the contribution of "direct+cascade" events is predominant, consisting of 98.4% (93.4% according to the simulation) of the total yield; the additional condition  $M_{inv} \subseteq [0:3]$  GeV is thus imposed to produce a sample of events enriched with

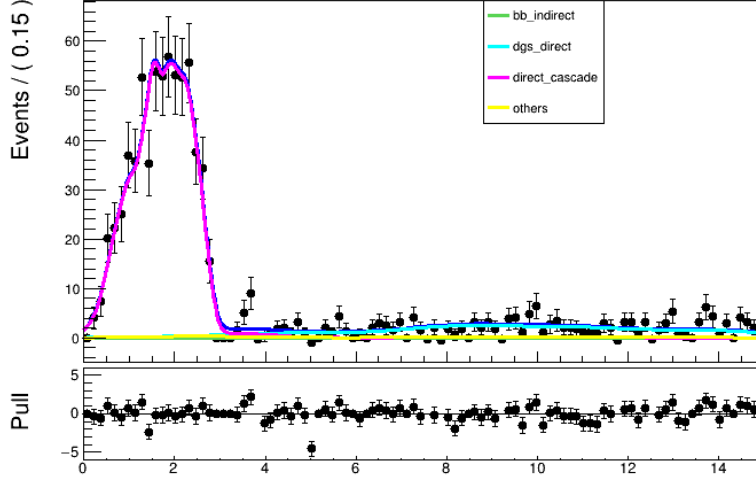


Figure 36: Fit of the variable  $M_{inv}$  for muon pairs with invariant mass smaller than 15 GeV. The data distribution is consistent with the simulation.

pairs made of a direct muon (the OC one) and the other that comes from a cascade decay. A fit is now performed on the  $\Psi_{SC}$  variable (i.e.  $\Psi$  for the non-direct muon) to check if the simulation correctly describes cascade muons. The results are shown in Fig.37 and in Tab.16; a good agreement between the distribution of data and simulation is obtained. The values of  $\Psi_{SC}$  are peaked at small values, as expected for background muons, but the categories fractions are not totally compatible. This could be due to the fact that all template distributions, except for the DGS one, are quite similar, so they could be easily confused in the fit. However, the most significant category is correctly identified as "direct+cascade".

Category	$M_{inv}$ fit in $M_{inv} \subseteq [0 : 15]$ GeV		$\Psi_{SC}$ fit in $M_{inv} \subseteq [0 : 3]$ GeV	
	Fit %	MC %	Fit %	MC %
$bb_{indirect}$	$(1.6 \pm 0.7) \cdot 10^{-4}$	2.2	0	2.7
$DGS_{direct}$	$17.4 \pm 0.4$	13.6	0	0.3
direct-cascade	$81.0 \pm 0.3$	68.2	100	93.4
others	$1.6 \pm 0.5$	16.0	0	3.6
Tot entries	1049	1343	819	942

Table 16: Relative contributions of different categories, extracted from the final coefficients of the fit and from the simulation. The results are shown in columns 2-3 for the  $M_{inv}$  fit and in columns 4-5 for the  $\Psi_{SC}$  fit. For cases in which the relative error on the fit parameters is smaller than  $10^{-5}$ , the error is not reported. The MC assignation of the entries instead are assumed exact, so no errors are associated to the computed fractions.

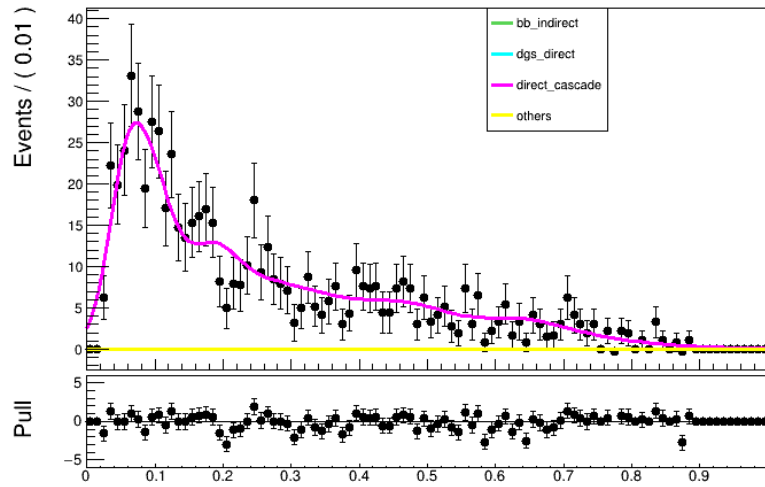


Figure 37: Fit of the variable  $\Psi_{SC}$  for muon pair with invariant mass smaller than 3 GeV. The data distribution is consistent with the simulation.

## B Pile-up analysis

In this section we describe a study of pile-up events, in which one (or more) muon(s) on the probe side come from two different interaction vertices.<sup>3</sup>

To reduce this background we apply a selection on the variable  $\Delta z = z_{prb} - z_{tag}$ , where  $z_{prb}$  is the coordinate along the  $z$  direction of the point where the muon track intersects the beam line;  $z_{tag}$  is obtained as the average position along  $z$  of the intersections of the three tracks forming the  $B_{tag}$  with the beam line. Signal events are defined as those that belong to the region  $|\Delta z| < 0.25$  cm.

However, from the  $\Delta z$  plots in Fig:38-39 we can see that the distributions of pile-up events is continuous and extends also in the signal region. To calculate the fraction of residual pile-up events in the signal region, we fit the total  $\Delta z$  distribution for probe muons with the function  $g(x)$ , defined as the sum of four gaussians, one for the background and three for the peak.

$$g(x) = \sum_{i=1}^4 C_i \exp \left\{ -\frac{1}{2} \left( \frac{x - \mu_i}{\sigma_i} \right)^2 \right\} \quad (4)$$

The background gaussian is defined as the one with the smallest constant parameter  $C_i$  and is plotted on the  $\Delta z$  distributions. Its integral in the region  $|\Delta z| < 0.25$  provides the number of residual pile-up events: their fraction is reported in Tab:17.

	OC	SC
signal+residual pile-up	195299 ± 442	91149 ± 302
residual pile-up	1488 ± 39	1489 ± 39
fraction of residual pile-up	(0.76 ± 0.02) %	(1.63 ± 0.04) %

Table 17: Fraction of residual pile-up contribution in the signal region.

As discussed in Sect:4.5.2, the  $\Delta\eta$  distribution for pile-up events is well represented by the templates defined by muons from charm, from  $\pi$  or  $K$  and from other sources, which are used as template for the "uncorrelated" muons. So, in the final fit the contribution of pile-up muon is absorbed in the "uncorrelated" category, without the need to explicitly count the number of direct muons among the residual pile-up events and to subtract them.

---

<sup>3</sup>Due to the huge cross section and large density of protons in the LHC bunches, in each beam intersection several proton proton collisions (about 30 on average) take place in different positions along the beam line ( $z$ ) and are recorded in a unique event: particles emerging from different vertices are created in different interactions and are not physically correlated with each other, so this is a source of background that affects our sample.

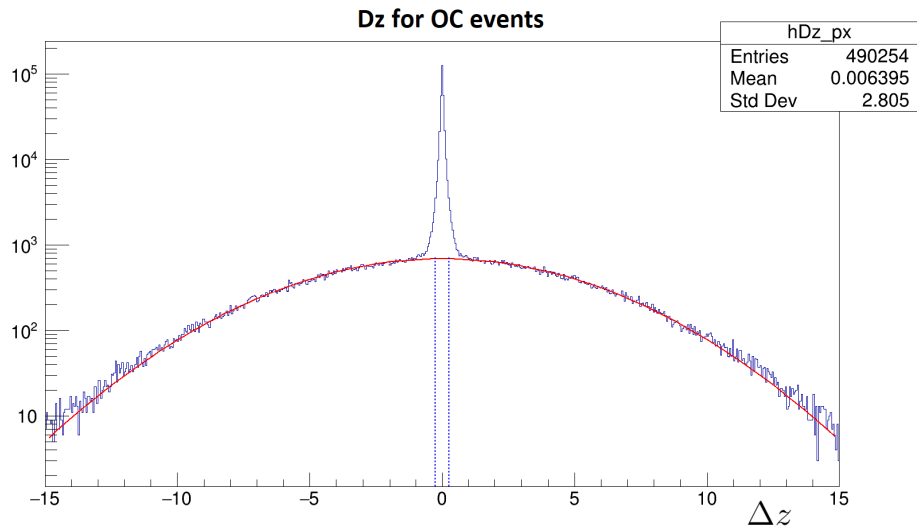


Figure 38:  $\Delta z$  distributions for OC events, with the plot of the background gaussian. The inner part of the blue lines is the  $\Delta z$  range that identifies residual pile-up events.

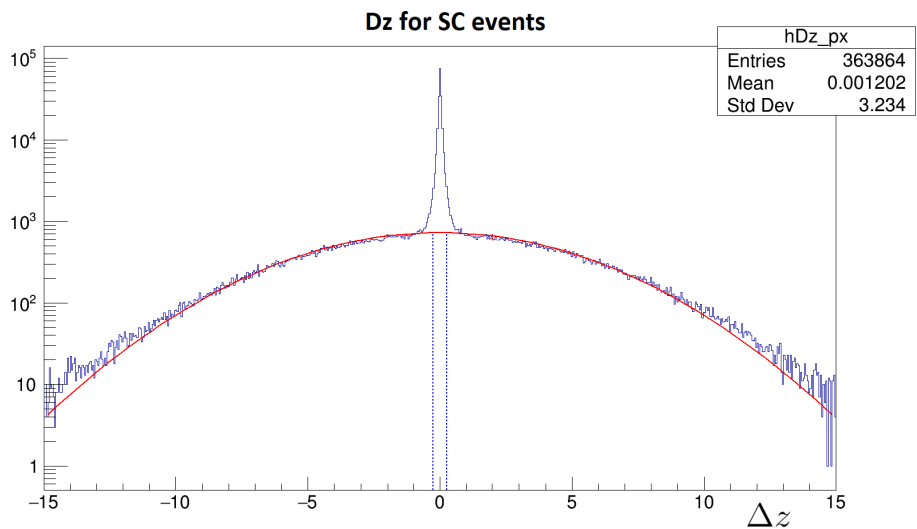


Figure 39:  $\Delta z$  distributions for SC events, with the plot of the background gaussian. The inner part of the blue lines is the  $\Delta z$  range that identifies residual pile-up events.

## C Multivariate Analysis (MVA)

The Toolkit for Multivariate Data Analysis (TMVA) is a ROOT-based framework that integrates many different multivariate classification and regression techniques. In the package the following classifiers are implemented: multi-dimensional likelihood estimation, linear and nonlinear discriminant analysis, support vector machine (SVM), deep neural network (DNN), boosted decision trees (BTD). The learning framework is the following:

- Domain set  $\mathcal{X} \subseteq \mathcal{R}^d$ : the set of objects that we wish to label, in this case all the muons on the probe side with their associated features (variables of the ntuple).
- Label set  $\mathcal{Y} = \{0, 1\}$ : the set of possible labels. In this case we want to perform a binary classification, i.e. to distinguish between signal (1) and background (0)
- Predictor  $h : \mathcal{X} \rightarrow \mathcal{Y}$ , one of the classifiers listed above.
- Training set  $S = \{(x_1, y_1) \dots (x_m, y_m)\}$ : a sequence of labeled domain points. For this analysis  $S$  is the simulated sample, where each point is labeled "signal" or "background".

The training and testing procedure are performed on the simulated events; after that, the multivariate discriminator is evaluated for both simulated and data points.

For the training and testing procedure Boosted Decision Trees (whose functioning is explained in C.1) are chosen, showing better separation performances with respect to other classifiers; their output is a series of weight files.

Within an event loop, a vector is filled with the variables that were used to train the MVA during the training stage. In the evaluation stage, the output vector is transferred to a reader who interprets the weight file and returns the MVA's output, the discriminator  $\Psi$ . Its continuous values are rescaled to the range  $[0:1]$ , where '0' refers to background and '1' to signal.

### C.1 Boosted decision trees

A decision tree [11] is a predictor,  $h : \mathcal{X} \rightarrow \mathcal{Y}$ , that predicts the label associated with an instance  $x \in \mathcal{X}$  by traveling from a root node of a tree to a leaf. At each node on the root-to-leaf path, the successor child is chosen on the basis of a splitting of the input space. Usually, the splitting is based on one of the features of  $x$  or on a predefined set of splitting rules. A leaf contains a specific label and the splitting rule at the internal nodes of the tree is based on thresholding the value of a single feature, as depicted in Fig:40. Without a stopping criteria a decision tree generally ends up overfitting. To avoid that, in TMVA the stop criteria for the splitting during the training phase is given by the minimum number of events that is required for a leaf node.

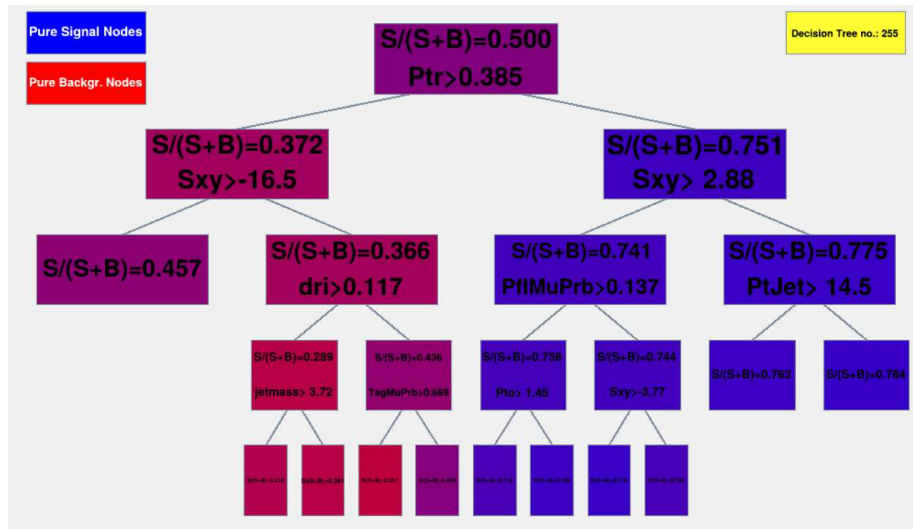


Figure 40: Example of a decision tree trained for this analysis.

## References

- [1] N. L. Johnson. “Systems of Frequency Curves Generated by Methods of Translation”. In: *Biometrika* 36.1/2 (1949), pp. 149–176. ISSN: 00063444, 14643510. URL: <http://www.jstor.org/stable/2332539> (visited on 08/05/2025).
- [2] Makoto Kobayashi and Toshihide Maskawa. “CP-Violation in the Renormalizable Theory of Weak Interaction”. In: *Progress of Theoretical Physics* 49.2 (Feb. 1973), pp. 652–657. ISSN: 0033-068X. DOI: 10.1143/PTP.49.652. eprint: <https://academic.oup.com/ptp/article-pdf/49/2/652/5257692/49-2-652.pdf>. URL: <https://doi.org/10.1143/PTP.49.652>.
- [3] Elisabetta Barberio, Bob van Eijk, and Zbigniew Was. “Photos — a universal Monte Carlo for QED radiative corrections in decays”. In: *Computer Physics Communications* 66.1 (1991), pp. 115–128. ISSN: 0010-4655. DOI: [https://doi.org/10.1016/0010-4655\(91\)90012-A](https://doi.org/10.1016/0010-4655(91)90012-A). URL: <https://www.sciencedirect.com/science/article/pii/001046559190012A>.
- [4] Bo Andersson. *The Lund Model*. Cambridge Monographs on Particle Physics, Nuclear Physics and Cosmology. Cambridge University Press, 1998.
- [5] David J. Lange. “The EvtGen particle decay simulation package”. In: *Nuclear Instruments and Methods in Physics Research Section A: Accelerators, Spectrometers, Detectors and Associated Equipment* 462.1 (2001). BEAUTY2000, Proceedings of the 7th Int. Conf. on B-Physics at Hadron Machines, pp. 152–155. ISSN: 0168-9002. DOI: [https://doi.org/10.1016/S0168-9002\(01\)00089-4](https://doi.org/10.1016/S0168-9002(01)00089-4). URL: <https://www.sciencedirect.com/science/article/pii/S0168900201000894>.
- [6] S. Agostinelli et al. “Geant4—a simulation toolkit”. In: *Nuclear Instruments and Methods in Physics Research Section A: Accelerators, Spectrometers, Detectors and Associated Equipment* 506.3 (2003), pp. 250–303. ISSN: 0168-9002. DOI: [https://doi.org/10.1016/S0168-9002\(03\)01368-8](https://doi.org/10.1016/S0168-9002(03)01368-8). URL: <https://www.sciencedirect.com/science/article/pii/S0168900203013688>.
- [7] Oliver Sim Brüning et al. *LHC Design Report*. CERN Yellow Reports: Monographs. Geneva: CERN, 2004. DOI: 10.5170/CERN-2004-003-V-1. URL: <https://cds.cern.ch/record/782076>.
- [8] Matteo Cacciari, Gavin P. Salam, and Gregory Soyez. “The anti-kt jet clustering algorithm”. In: *Journal of High Energy Physics* 2008.04 (Apr. 2008), p. 063. DOI: 10.1088/1126-6708/2008/04/063. URL: <https://dx.doi.org/10.1088/1126-6708/2008/04/063>.
- [9] *The CMS Collaboration et al 2008 JINST 3 S08004*. 2008. DOI: 10.1088/1748-0221/3/08/S08004. URL: <https://iopscience.iop.org/article/10.1088/1748-0221/3/08/S08004/pdf>.

- [10] R Aaij et al. “Precision measurement of the  $B_0$ s oscillation frequency with the decay  $B_0 \rightarrow D_s^+$ ”. In: *New Journal of Physics* 15.5 (2013). ISSN: 1367-2630. DOI: 10.1088/1367-2630/15/5/053021. URL: <http://dx.doi.org/10.1088/1367-2630/15/5/053021>.
- [11] Shai Shalev-Shwartz; Shai Ben-David. *Understanding Machine Learning, from theory to algorithms*. Cambridge University Press, 2014.
- [12] A Benaglia. “The CMS ECAL performance with examples”. In: (2014). DOI: 10.1088/1748-0221/9/02/C02008.
- [13] “Performance of the CMS muon detector and muon reconstruction with proton-proton collisions at  $\sqrt{s} = 13\text{TeV}$ ”. In: (2015). DOI: 10.1088/1748-0221/13/06/P06015.
- [14] Torbjörn Sjöstrand et al. “An introduction to PYTHIA 8.2”. In: *Computer Physics Communications* 191 (2015), pp. 159–177. ISSN: 0010-4655. DOI: <https://doi.org/10.1016/j.cpc.2015.01.024>. URL: <https://www.sciencedirect.com/science/article/pii/S0010465515000442>.
- [15] R. Aaij et al. “A precise measurement of the  $B_0$  meson oscillation frequency”. In: *The European Physical Journal C* 76.7 (2016). ISSN: 1434-6052. DOI: 10.1140/epjc/s10052-016-4250-2. URL: <http://dx.doi.org/10.1140/epjc/s10052-016-4250-2>.
- [16] R.D. Ball, V. Bertone, and S. Carrazza. “Parton distributions from high-precision collider data”. In: *The European Physical Journal C* (2017). DOI: <https://doi.org/10.1140/epjc/s10052-017-5199-5>. URL: <https://link.springer.com/article/10.1140/epjc/s10052-017-5199-5#citeas>.
- [17] A.M. Sirunyan et al. “Particle-flow reconstruction and global event description with the CMS detector”. In: *Journal of Instrumentation* 12.10 (Oct. 2017), P10003–P10003. ISSN: 1748-0221. DOI: 10.1088/1748-0221/12/10/p10003. URL: <http://dx.doi.org/10.1088/1748-0221/12/10/p10003>.
- [18] *The Phase-2 Upgrade of the CMS Tracker, Technical Design Report*. 2017. URL: <https://cds.cern.ch/record/2272264/files/CMS-TDR-014.pdf>.
- [19] R Bruce et al. “Review of LHC Run 2 Machine Configurations”. In: (2019), pp. 187–197. URL: <https://cds.cern.ch/record/2750415>.
- [20] Martina Ressegotti. “Overview of the CMS Detector Performance at LHC Run 2”. In: *Universe* 5.1 (2019). DOI: 10.3390/universe5010018.
- [21] R. Aaij et al. “Measurement of  $f_s/f_u$  Variation with Proton-Proton Collision Energy and  $B$ -Meson Kinematics”. In: *Phys. Rev. Lett.* 124 (12 Mar. 2020), p. 122002. DOI: 10.1103/PhysRevLett.124.122002. URL: <https://link.aps.org/doi/10.1103/PhysRevLett.124.122002>.

- [22] A.M. Sirunyan and A. Tumasyan. “Extraction and validation of a new set of CMS pythia8 tunes from underlying-event measurements”. In: *The European Physical Journal C* (2020). DOI: <https://doi.org/10.1140/epjc/s10052-019-7499-4>. URL: <https://link.springer.com/article/10.1140/epjc/s10052-019-7499-4#citeas>.
- [23] Y. Amhis et al. “Averages of b-hadron, c-hadron, and -lepton properties as of 2018”. In: *The European Physical Journal C* (2021). URL: <https://link.springer.com/article/10.1140/epjc/s10052-020-8156-7#citeas>.
- [24] A. Bragagnolo. “Measurement of the CP-violating phase  $\phi_{\text{hs}}$  with muon-tagged  $B_s \rightarrow J/\Psi \phi$  decays”. In: (2021).
- [25] Stefano Catani et al. “Bottom-quark production at hadron colliders: fully differential predictions in NNLO QCD”. In: *Journal of High Energy Physics* 2021.3 (2021). ISSN: 1029-8479. DOI: 10.1007/jhep03(2021)029. URL: [http://dx.doi.org/10.1007/JHEP03\(2021\)029](http://dx.doi.org/10.1007/JHEP03(2021)029).
- [26] A.M. Sirunyan et al. “Measurement of the CP-violating phase  $\phi_s$  in the  $B_s^0 \rightarrow J/\Psi \phi(1020) \rightarrow \mu^+ \mu^- K^+ K^-$  channel in proton-proton collisions at  $\sqrt{s} = 13$  TeV”. In: *Physics Letters B* 816 (2021). ISSN: 0370-2693. DOI: 10.1016/j.physletb.2021.136188. URL: <http://dx.doi.org/10.1016/j.physletb.2021.136188>.
- [27] E. Lusiani. “Flavor tagging algorithms for CP violation measurements in CMS”. In: (2023). URL: <https://hdl.handle.net/11577/3508267>.
- [28] Francesco Silvan. *Misura della violazione di CP indotta dall’oscillazione dei mesoni B: studio di fattibilità con i dati parked di CMS*. 2023. URL: <https://hdl.handle.net/20.500.12608/61009>.
- [29] A. Tumasyan et al. “Measurement of the Dependence of the Hadron Production Fraction Ratios”. In: *Physical Review Letters* 12 (2023). DOI: 10.1103/physrevlett.131.121901. URL: <http://dx.doi.org/10.1103/PhysRevLett.131.121901>.
- [30] *HFLAV 2024 averages*. 2024. URL: [https://hflav-eos.web.cern.ch/hflav-eos/osc/HFLAV\\_2024/#DMD](https://hflav-eos.web.cern.ch/hflav-eos/osc/HFLAV_2024/#DMD).
- [31] S. Navas et al. “Review of particle physics”. In: *Phys. Rev. D* 110.3 (2024), p. 030001. DOI: 10.1103/PhysRevD.110.030001.
- [32] *Particle Data Group*. 2024. URL: [https://pdg.lbl.gov/2024/listings/contents\\_listings.html](https://pdg.lbl.gov/2024/listings/contents_listings.html).
- [33] Neutelings I. *CMS coordinate system*. URL: [https://tikz.net/axis3d\\_cms/](https://tikz.net/axis3d_cms/).